A comparison between hydrothermal alteration present in the Vargeão Dome and Vista Alegre impact structures (Brazil) and CRISM remote sensing data from impact structures on Mars

Donna Dieperink
2640649

Research Project Geology and Geochemistry
AM_1267
Vrije Universiteit Amsterdam
Faculty of Science

14-07-2023

PhD(c) J. Alsemgeest
Vrije Universiteit Amsterdam
j.alsemgeest@vu.nl

Dr. F. Brouwer
Vrije Universiteit Amsterdam
fraukje.brouwer@vu.nl

Dr. M. Sanchez Roman
Vrije Universiteit Amsterdam
m.sanchezroman@vu.nl

Abstract

Impact-generated hydrothermal systems are considered a possible habitat for early life and are therefore of importance for the search of Martian life. To assess possible (past) impact-generated hydrothermal systems in Martian impact structures, two analogue structures on Earth, the Vargeão and Vista Alegre impact structures in Brazil, were compared to four Martian impact craters: Toro, Auki, Laylá, and Canso.

Hydrothermal alteration, consisting of zeolites, celadonite and beidellite, in the Brazilian analogues was observed using hyperspectral data, in combination with optical and scanning electron microscopy data. Based on these data, a decision tree was developed to classify individual minerals. This decision tree was then applied to hyperspectral remote sensing data of the Martian craters.

The classification of Toro crater shows clear signals of hydrous minerals: illite, celadonite, and beidellite(?). Other craters lack these signals. This lack of signals can be explained by shortcoming in (pre-)processed CRISM data and in the decision tree, differences in topographical resolution, dust cover, different origin of these hydrous minerals and differences in Martian and terrestrial hydrothermal systems.

The developed decision tree is well applicable to terrestrial samples and CRISM data containing hydrothermal alteration, but must be combined with other methods to get a complete overview of hydrothermal alteration.

Within the limitations of this study, a minimum crater size for an impact-generated hydrothermal system to occur on Mars is estimated around 30-40 km.

Impact-generated hydrothermal systems most likely explain the occurrence of hydrous minerals in Martian craters, because the suggested impact-generated hydrous mineral, illite, is observed in Toro crater, while zeolites, which are likely excavated, are not observed in selected Martian craters.

Table of Contents

1. Introduction

1.1 Background

The human species has started looking for evidence of extraterrestrial life in the past few decades (Sagan, 1994). Because of the discovery of extremophile organisms, like microbial communities in black smokers, our view on the necessities of life has changed (Baross & Deming, 1983). Furthermore, this survival and possible origin of life in hostile environments brightened prospects in exobiology (Martin et al., 2008).

A potential candidate for the origin and sustenance of life during its early evolution is impact craters (Cockell et al., 2003). Due to conversion of kinetic to thermal energy during impact, heat releases into the substrate and atmosphere (Pirajno, 1992). The presence of water in the target rock and heat release can cause a hydrothermal system, in which hot fluids circulate in the subsurface (Pirajno, 2009; Yokoyama et al., 2015). Hydrothermal circulation is focused at sub-crater levels, but can extend to kilometers below the crater floor after an impact event (Komor et al., 1988). On Earth, hydrothermal activity has been confirmed in almost half of the impact craters (Osinski et al., 2013). Because hydrothermal systems cause availability of water, heat, dissolved chemicals, and nutrients, they are considered a possible habitat for early life and are therefore of importance not only for the origin and evolution of life on Earth, but also on other planets (Chatterjee, 2016; Osinski et al., 2013). The Martian surface is covered in impact craters, in which impact-generated hydrothermal systems could be present (Cockell, 2006). Data collected by the Compact Reconnaissance Imaging Spectrometer for Mars (CRISM) instrument comprise mineral assemblages on the southern highlands of Mars that suggest a diversity of past aqueous environments, including signs of hydrated materials (Wray et al., 2009). However, it is not clear whether the observed hydrothermal alteration in Martian impact craters have an impact-origin and if life could have originated in these systems. Due to sampling limitations on Mars, analogue impact craters on Earth may provide important insight in the existence and characteristics of impact-generated hydrothermal systems on Mars. Analogues on Earth are rare, as the composition of the Martian crust is mainly basaltic and only very few impact craters in basaltic target terrain exist on Earth (Alsemgeest et al., 2021; McSween et al., 2009). The Vargeão Dome and Vista Alegre impact structures in Brazil are in mainly basaltic target terrain, exposed and well accessible, and are therefore suitable analogues for Martian impact craters (Alsemgeest et al., 2021; Dypvik et al., 2021).

1.2 Goal

The goal of this project is to compare hyperspectral data of the Brazilian analogues with hyperspectral remote sensing data of impact structures on Mars to assess the likelihood that (past) impact-generated hydrothermal systems exist on Mars and find answers to the following questions. What hydrothermal alteration is present in samples from the Vargeão and Vista Alegre impact structures and how can this be recognized in hyperspectral data? How do the CRISM data and hyperspectral data from the Brazilian analogues compare?

1.3 Hydrothermal alteration

Hydrothermal alteration can be an indicator of the presence of a hydrothermal system. Therefore, hydrothermal alteration can be studied for the search for these life supporting systems on Mars. When rocks interact with circulating aqueous fluids in a hydrothermal system, complex processes involving chemical, textural, and mineralogical changes can occur (Pirajno, 2009). These changes are defined by hydrothermal alteration and can occur under subsolidus conditions after infiltration by a fluid in a rock mass (Pirajno, 2009). This process is a form of metasomatism between the fluids and rocks (Pirajno, 1992). Hydrothermal alteration is controlled by the nature of the rock mass, such as permeability, composition of the fluids, and temperature (Henley & Ellis, 1983; Pirajno, 1992). An increase in

hydrothermal alteration occurs at higher water/rock ratios (Pirajno, 2009). Therefore, observations of the amount of hydrothermal alteration could suggest the size of a hydrothermal system.

1.3 Brazilian impact structures

1.3.1 Analogues

To find a suitable analogue on Earth for Martian impact structures geologic, gravitational, and atmospheric differences between Mars and Earth have to be taken into account. Basaltic rocks dominate the Martian surface (Taylor et al., 2010). Therefore the analogue has to be located in a dominantly basaltic target domain. Only four craters on Earth that meet this condition are known: Lonar Lake in India, Logancha in Russia, and Vargeão Dome and Vista Alegre in (Crósta et al., 2010; Feldman et al., 1983; Fredriksson et al., 1973; Masaitis, 2010). The Vargeão Dome and Vista Alegre impact structures are exposed and well accessible, while Lonar lake is filled with hyposaline water and Logancha is poorly exposed and located in poorly accessible terrain in Siberia (Anoop et al., 2013). The surface of Mars contained abundant water in its early history (~3.8 Ga), based on present rocks and minerals, geomorphologic characteristics, and data from probe and rover missions (Nazari-Sharabian et al., 2020). Only a small part of this water is found nowadays in the form of (subsurface) ice or in water-rich minerals (Nazari-Sharabian et al., 2020). The analogue for Martian impact craters that formed after the aqueous period (~4 Ga-3.5 Ga) should thus be formed in a relatively dry environment (Fairén et al., 2010; Schwenzer et al., 2012). The Vargeão and Vista Alegre impact structures have a semi-arid climate and therefore meet this requirement (Alvares et al., 2013; Arújo et al., 1999). Mars has a much lower surface gravity and surface pressure than Earth, which results in different impacts from meteorites of the same size (Leovy, 2001). The characteristic size that differs craters with a simple from a complex form is ~3 km in diameter for Earth and ~6 km for Mars (Pike, 1980). This difference in impact form is also represented in the formation of a hydrothermal system. On Earth a hydrothermal system is likely to form in craters with a diameter of ~5 to 150 km and on Mars of ~10 to 250 km (Fig. 1.1) (Osinski et al., 2013). The Vista Alegre and Vargeão impact structures both fit in the range for Earth to have a possibility of the origin of a hydrothermal system. Because of gravitational and target differences between Earth and Mars, the Brazilian analogues with diameters around ~10 km compare to Martian impact craters with a diameter in the range of ~20-40 km (Osinski et al., 2013). Besides differences in the atmospheric pressure between Mars and Earth, there are also differences in the composition (Table 1.1) (Larsen et al., 2002). This could influence the types of impact-generated hydrothermal alteration, as different elements can be incorporated.

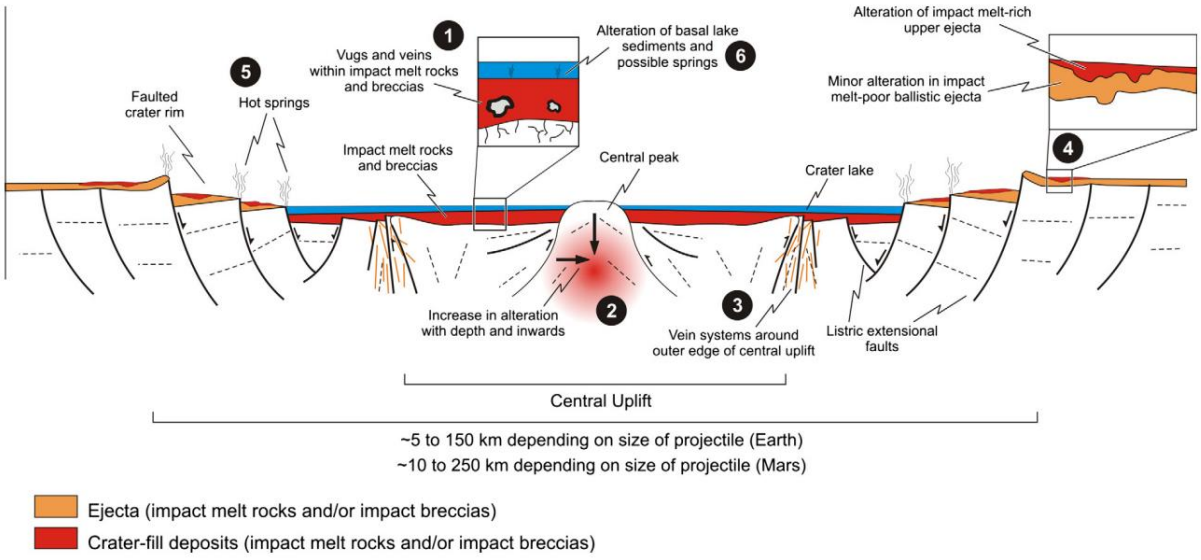

Fig. 1.1 Schematic overview of impact-generated hydrothermal alteration in a complex impact crater (Osinski et al., 2013).

Table 1.1 Composition of the atmosphere on Mars and on Earth in percentages by volume (%) (Larsen et al., 2002).

Component	Mars (0.007 atm)	Earth (1 atm)
CO_2	95	0.035
N_2	2.7	78
O_2	0.13	21
H_2O	0-0.2	0-4
Ar	1.6	0.9

1.3.2 Vargeão Dome

The 12.4 km wide Vargeão Dome formed between ~111 Ma and 134 Ma through an impact in Early Cretaceous volcanic rocks of the Serra Geral Group within the Paraná Basin in the south of Brazil (26°49'S and 52°10'W) (Fig. 1.2) (Crósta et al., 2011; Yokoyama et al., 2015). The structure shows a 3 km-wide central uplift of approximately 1100-1200 m that led to exposure of sandstones of the Botucatu and Pirambóia formations (Fig. 1.3) (Crósta et al., 2011). The impact origin of the structure is interpreted from shock features, like shatter cones, feather features, and diaplectic feldspar glass (Crósta et al., 2011). Breccia veins containing oxides, as well as locally glassy remnants and secondary minerals, developed in the basalts in the Vargeão Dome as a result of shock deformation (Yokoyama et al., 2015); the secondary minerals formed as a result of limited hydrothermal alteration (Yokoyama et al., 2015). The Vargeão Dome formed during a period with little to no precipitation and with the possible presence of the Guaraní aquifer that extends from the Botucatu to the Piramboia formations (Gonçalves et al., 2020). As hydrothermal circulation is not limited to the crater floor after impact, this aquifer can be a water source for a hydrothermal system (Komor et al., 1988; Yokoyama et al., 2015). Therefore, Vargeão Dome is one of the best analogs on Earth of dry Martian surface environments with presence of ground ice (Yokoyama et al., 2015). There is no decisive evidence that the impact event triggered formation of a large hydrothermal system and the observed mineral assemblages may result from excavation of pre-impact alteration of the basalts or post-impact chemical evolution (Alsemgeest et al., 2021; Yokoyama et al., 2015).

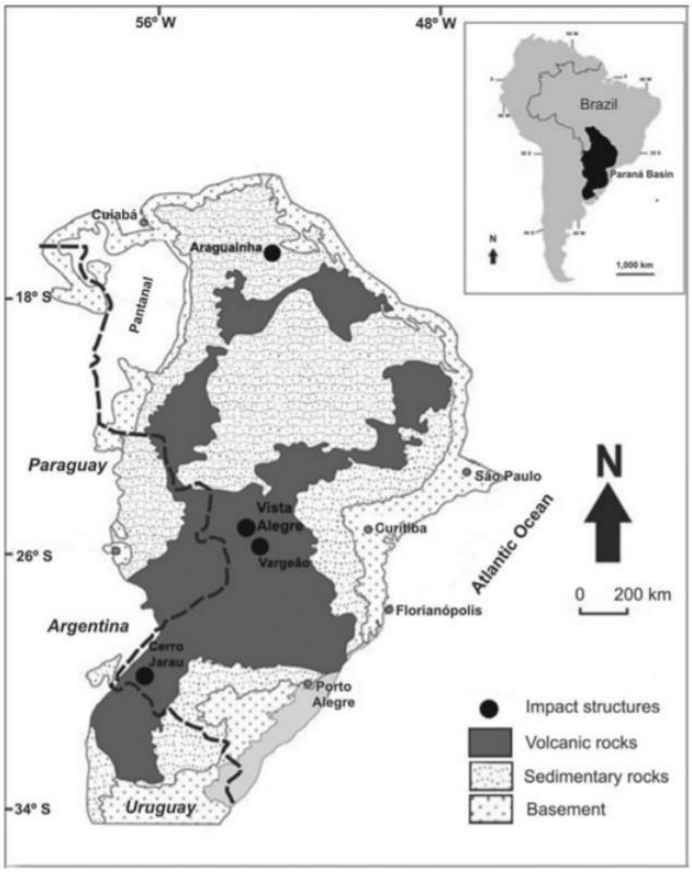

Fig. 1.2 Location of the Paraná Basin and the present impact structures (Crósta et al., 2010).

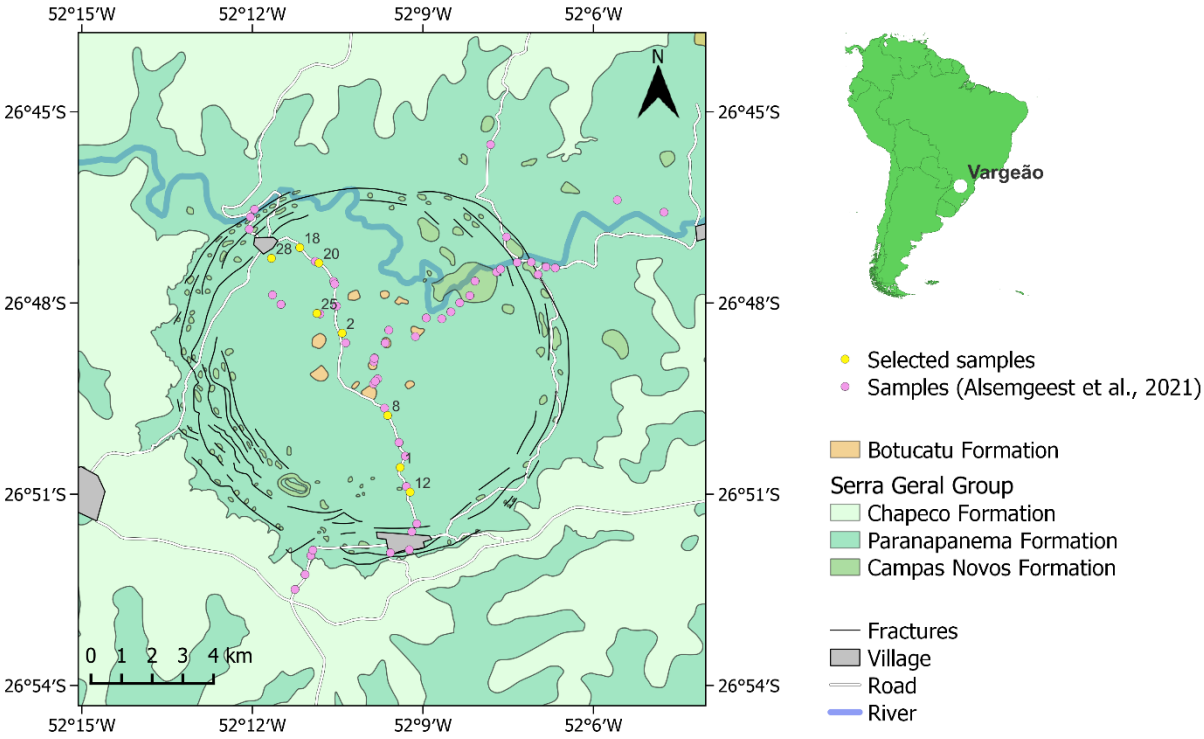

Fig. 1.3 Simplified map of the Vargeão Dome showing selected sample locations, annotated with numbers, the locations of the complete sample set, and the main geologic and topographic features (Alsemgeest et al., unpuplished).

1.3.3 Vista Alegre impact structure

The 9.5 km wide Vista Alegre impact structure is located at 25°57'S and 52°41'W (Crósta et al., 2010), about 100 km north-east of the Vargeão Dome in the Paraná Basin (Fig. 1.2) (Vasconcelos et al., 2019). This impact occurred between 111 and 134 Ma in the Paraná flood basalts of the Serra Geral Group and shows a central uplift of about 700-800 m of Triassic Botucatu/Piramoìa sandstones (Fig. 1.4) (Crósta et al., 2010; Vasconcelos et al., 2019). Due to extensive agriculture there are limited outcrops in the impact structure (Crósta et al., 2010). The presence of shatter cones and planar deformation features in quartz grains support the suggested impact origin of the Vista Alegre structure (Crósta et al., 2010). Similar to the Vargeão Dome, an aquifer was likely present during impact (Alsemgeest et al., 2021). Three types of hydrothermal alteration have been observed that were all located within a 2.5-3 km radius of the impact crater center: two sets of hydrothermal veins consisting predominantly of calcite and chabazite, and local alteration features, mostly containing saponite (Alsemgeest et al., 2021). These types of alteration do not indicate the existence of a large impact-generated hydrothermal system and are more likely excavated material (Alsemgeest et al., 2021). It is possible that quartzites with relatively low permeability and porosity are present in the Botucatu/Piramoìa sandstones (Crósta et al., 2011). This may limit the access of water to volcanic rocks of the Serra Geral Formation in the impact structure, which could explain the lack of evidence for an impact-generated hydrothermal system (Alsemgeest et al., 2021).

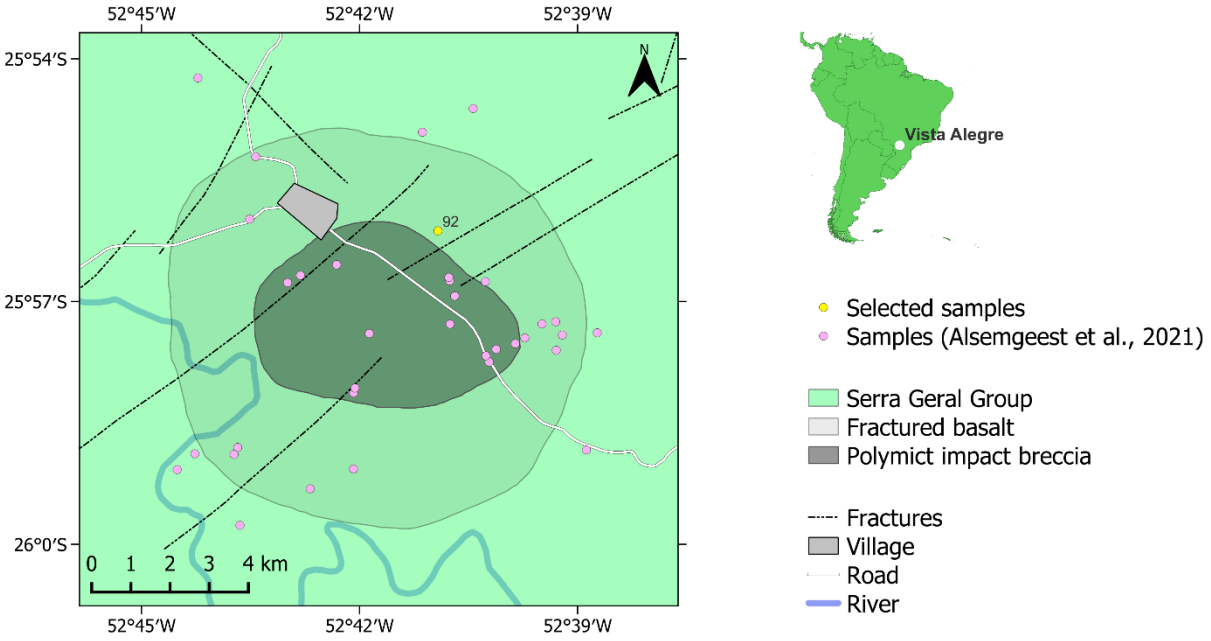

Fig. 1.4 Simplified map of the Vista Alegre impact structure showing selected samples locations, annotated with numbers, the locations of the complete sample set, and the main geologic, lithologic, and topographic features (Alsemgeest et al., 2021).

1.4 Martian research areas

1.4.1 Hydrothermal alteration on Mars

Hydrous minerals have been observed in different areas on Mars using hyperspectral images (Carter et al., 2013; Fairén et al., 2010; Rathbun & Squyres, 2002; Schwenzer et al., 2012; Wray et al., 2009). These are concentrated in the southern highlands and cover about 3% of the Martian surface (Carter et al., 2013). Phyllosilicates, zeolites and sulfates are exposed across the Noachian southern highlands of Mars, which suggest a great variety of past aqueous environments on Mars (Wray et al., 2009). Chlorite and analcime are observed in impact craters with a diameter of tens of kilometers in the areas Noachis and Cimmeria Terrae (Fig. 1.5) (Wray et al., 2009). Clays are observed in the crater walls and ejecta of small craters <1 km in Noachis and Sirenum Terrae, which are likely to have a pre-impact origin (Rathbun & Squyres, 2002; Wray et al., 2009). Furthermore, polyhydrated sulfates are observed in the Central Noachis Terra and in the Sisyphi Montes (Fig. 1.5) (Wray et al., 2009).

In the northern lowlands of Mars hydrous minerals have also been found. These are observed in excavated material of impact craters in the lowlands (Carter et al., 2013). These minerals are presumably pre-impact and originated in the Noachian-aged basement, as no hydrous minerals were found in craters, which were too small for excavation of material (Carter et al., 2013). Of these hydrous minerals, phyllosilicates have been observed in all Noachian-aged units and impact craters, in which excavation occurred (Carter et al., 2013).

However, there are also Martian areas that lack evidence of hydrous minerals, such as the Promethei Terra and southern or northeast Cimmeria Terra (Fig. 1.5). Dust cover on Mars could possibly explain the impossibility of observing these minerals in these areas (Wray et al., 2009). Observations on the absence of hydrous minerals have been taken into account with selecting Martian research areas in this project (section 1.4.2).

1.4.2 Martian impact craters

Four Martian impact craters have been selected: Auki, Canso, Laylá and Toro crater. These are located in the Martian Highlands and have been selected to compare with Vista Alegre and Vargeão after assessing the quality of the available CRISM data of all craters (section 2.4). The craters have been selected to fit into a diameter range of 20-42 km (section 1.3.1). Estimated ages of the impact events

have a broad range to indicate the influence of erosion and dust cover on the possibility of observing hydrothermal alteration. Besides a fit in the diameter range, Toro and Auki were selected based on earlier observations of hydrous minerals and Canso and Laylá based on the good quality of the CRISM images (section 2.4) (Carrozzo et al., 2017; Fairén et al., 2010). The structures are described in detail below.

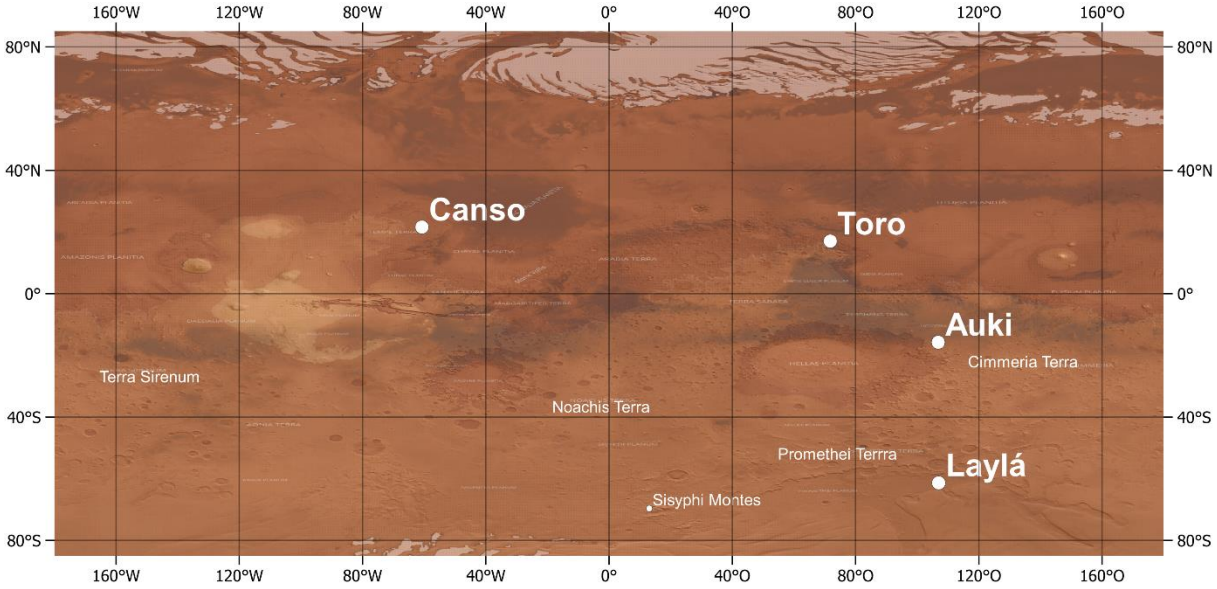

Fig. 1.5 Map with Martian terrains and features, and selected impact craters to compare with the Vista Alegre and Vargeão impact structures.

Auki

The Auki crater with a diameter of ~38 km is located in the Tyrrhena Terra , 15.7 °S and 96.8 °E (Fig. 1.5) (Carrozzo et al., 2017). The central peak and elevation on the edge of the crater are clearly visible on Context Camera (CTX) images, but there are no quantitative estimates of these heights (Fig. 1.6.A). Crater ejecta are visible until 60 km from the crater center (Carrozzo et al., 2017). These are signals of a relatively young crater with little infill. Smectite, silica, zeolite, serpentine, carbonate, and chlorite have been observed using CRISM data (Carrozzo et al., 2017). Hydrous minerals located around the central uplift are likely related to excavation during impact (Carrozzo et al., 2017). The correlation between the hydrous minerals with morphological structures, such as mounds, polygonal terrains, fractures and veins suggests that these are formed as a result of an impact-generated hydrothermal system (Carrozzo et al., 2017). The origin of water for a hydrothermal system is from underground circulation or the melting of ice, as there are no signs of surface water in the crater morphology (Carrozzo et al., 2017). However, an excavation origin of the observed hydrous minerals cannot be excluded (Carrozzo et al., 2017).

Canso

The Canso crater with a diameter of ~27.4 km is located northeast of the Lunae Planum and west of the Chryse Planitia, 21.6°N and 60.7°W (Fig. 1.5) (Kieffer et al., 1992). The Canso crater has a clear central peak and elevation near the edges of the crater, but the heights of these features are not quantitatively specified (Fig. 1.6.B). The clear presence of these features indicates likeliness of a relatively young origin, but no estimates are present in literature. The presence and origin of hydrous minerals have not been previously studied in this crater.

Laylá

The Laylá crater with a diameter of 20.8 km is located in the Promethei Terra, 61.35°S and 117.0°E (Fig. 1.5). The central uplift and elevation at the edges of the crater are less clearly visible compared to Canso crater and could indicate infill of the crater with dust and a relatively old age (Fig. 1.6.B/C).

However, there are no studies into the Laylá crater and age data are not known. Therefore, information on the presence and origin of hydrous minerals in Laylá crater is also lacking.

Toro

The Toro crater with a diameter of 42 km is located in the north of the Syrtis Major Volcanic Plains, 17.0°N and 71.8°E, in the highlands of Mars (Fig. 1.5) (Fairén et al., 2010). The central peak and elevation at the edge of the crater are relatively well visible and the crater has a depth of ~2 km (Fig. 1.6.D). The crater has an estimated age of 3.6 ± 0.1 Ga using crater counting, which means the impact occurred during the Hesperian (Fairén et al., 2010). The crater also shows a lobate outer margin (Fig. 1.6.D). This outer margin could indicate a rampart crater, in which material moved along the surface after impact instead of flying up and down. These mudflows suggest the melting of subsurface ice (Stewart et al., 2001). Hydrated and hydroxylated silicates are observed from hyperspectral data (Fairén et al., 2010). Some Hesperian or younger aged phyllosilicates that occurred well after the wet Early Noachian are suggested to be formed by Hesperian impact-generated hydrothermalism (Fairén et al., 2010).

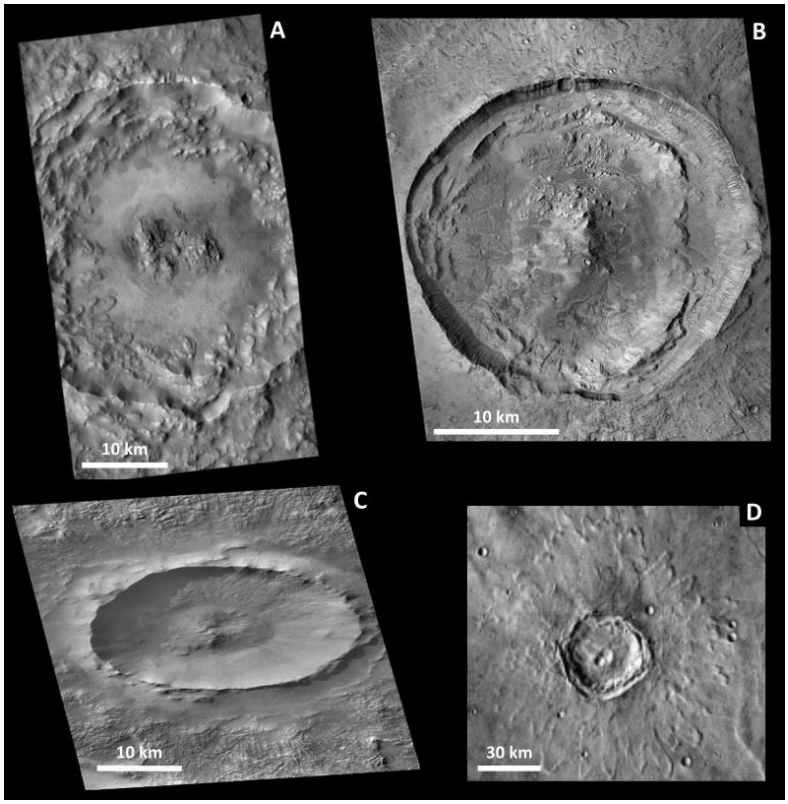

Fig. 1.6 CTX images of A. Auki; B. Canso; C. Laylá and D. Toro (Malin et al., 2007).

2. Methods

To indicate the presence of fossil impact-generated hydrothermal systems on Mars, the Vista Alegre, and Vargeão impact structures in Brazil were compared to Martian impact structures. Hydrothermal alteration was analyzed with optical and scanning electron microscopy in samples of the Brazilian structures. Spectroscopic images of the samples were linked to the observed hydrothermal alteration and compared to available, remote spectroscopic data form Mars, CRISM data, to indicate the presence of similar hydrothermal alteration in Martian impact structures and suggest the possibility of presence of hydrothermal systems in these craters.

2.1 Sample selection

Samples were selected from an available sample set of the Vargeão Dome and Vista Alegre impact structures, which were collected during a field excursion in October 2019 and were previously analyzed in Alsemgeest et al. (2021). This sample set consists of thin sections and rock slices from 56 outcrops in the Vargeão Dome (VG1 t/m VG56) and 36 outcrops in the Vista Alegre impact structure (VA57 t/m VA92) (Fig. 1.3/4 and Table A.2.4). All samples containing signals of hydrothermal alteration, as well as 5 breccias, a sandstone (4B), and 3 rock samples without alteration were selected for optical microscopy (Table 2.1). Samples with uncertainties in mineral content were further analyzed using Scanning Electron Microscopy (SEM) (section 2.2 and Table 2.1). Both samples with and without signs of hydrothermal alteration were spectroscopically imaged (Table 2.1). Samples VG1A, VG2, VG8, VG12, VG18, VG20, VG25, VG28B and VA92 were selected to represent the complete observed variation, as these contain distinct examples of hydrothermal alteration (Table A.2.2/4).

Table 2.1 Overview of performed analysis on the sample set. Samples representative of the hydrothermal alteration in the Vargeão and Vista Alegre impact structures marked in green.

Sample	Optical microscopy	SEM	Spectroscopic imaging
Vargeão			
1A	*		*
1B	*	*	*
1C			*
2	*		*
4A			*
4B	*		
6	*		*
8	*	*	*
9	*	*	*
12	*	*	*
14	*	*	*
15			*
16			*
18	*	*	*
20	*	*	*
21			*
24	*		
25	*	*	*
25B	*		*
28A	*		
28B	*		*
33	*	*	*
34	*	*	*
35A	*		*
35B			*
40	*		
47A	*		*
47B			*
48	*	*	*
51	*	*	*
53	*	*	*
56	*		*
Vista Alegre			
75			*
78			*
80A	*	*	
92	*	*	*

2.2 Optical and scanning electron microscopy

Thin sections of the selected rock samples were analyzed for different signs of hydrothermal alteration using a Zeiss Axiolab 5 at the Vrije Universiteit. The mineralogic content of veins and the basaltic matrix is interpreted based on color, cleavage, crystal shape, and interference color. Photographs were taken using the camera of the Zeiss Axiolab 5 of veins for comparison between different rock samples. The samples were further analyzed using a JEOL JCM-6000 benchtop Scanning Electron Microscope (SEM) and methods described in Alsemgeest et al. (2021) at the Microanalysis Laboratory at Vrije Universiteit Amsterdam, with focus on unclear features observed with optical microscopy. Backscattered Electron (BSE) images were taken and Energy Dispersive X-ray Spectroscopy (EDS) data were collected from the veins and matrix. Because of great similarities in hydrothermal alteration features, not all samples were further analyzed using SEM (Table 2.1 and section3.2).

2.3 Spectroscopic imaging

2.3.1 Imaging

Short-wave infrared (SWIR) data from selected samples were collected in the Spectroscopy Laboratory of the University of Twente. The hyperspectral data were measured by using the Specim Hyperspectral camera with a spectral resolution of 12 nm. This camera measures in 288 spectral bands with a spectral precision of 5.7 nm. Per rock sample 3-6 slices of 384 spatial pixels, pixel size: 26 x 26 µm, were measured. The image data consist of a flat-binary raster file with an accompanying ASCII header file. Before the hyperspectral images are acquired, the sample layout on the tray is photographed for later reference. The hyperspectral slices per rock sample overlap to allow for mosaicking to form a spectroscopic image of the complete rock samples (section 2.3.2).

2.3.2 Processing

Processing and mosaicking

Initial processing steps and mosaicking is performed to the collected SWIR data, using the Hyperspectral Python package (Hyppy3), designed to process hyperspectral images (Bakker, 2018), the Orfeo Toolbox, designed to process remote sensing images (Grizonnet et al., 2017) and QGIS (QGIS_Development_Team, 2023). Hyperspectral data slices were processed using the Dark and White Reference tool in Hyppy3. The dark and white referenced images were then cropped using the Subset/Convert tool in Hyppy3 to fit the other slices per rock sample. Using the Tile Fusion tool in the Orfeo Toolbox different data slices were mosaicked together and saved as a TIF file (Grizonnet et al., 2017). In QGIS these TIF files were added as a raster layer and exported as an ENVI.hdr labelled file, consisting of an ENVI file and a header file with metadata (Buller, 2023; QGIS_Development_Team, 2023).

Image quality improvement and formation of wavelength maps

The mosaicked files were further processed to improve the hyperspectral image quality and editing options. Bands 1-16 and 188 were removed using “Resize Data (Spatial Spectral)” from the “Basic Tools” in ENVI. The tool destripefilt in Hyppy 3 was used to remove bad pixels and band names in the header file were removed to allow for the processing of results. The mean 7 filter was applied to the hyperspectral images in Hyppy 3 to smooth the spectra. After these edits to improve the quality of the spectroscopic image an albedo calculation was made using “Log/Kwik Residuals” in “Tools” in Hyppy 3 to improve the visibility of the texture. . The “Median 9+9+9 neighborhood” tool in the spectral median filter of Hyppy3 was used to smooth the data. Finally, wavelength maps were created using “Step 1 – Wavelength of minimum” and “Step 2 – Wavelength Mapping” in Hyppy 3 for wavelength ranges 1000-1500 nm, 1300-1600 nm, 1650-1850 nm, 1850-2100 nm, 2000-2500 nm and 2100-2400 nm.

Mineral (group) classification of hydrothermal data

To classify hydrothermal alteration observed in the Vista Alegre and Vargeão samples a decision tree was designed using differences in absorption features of the observed minerals. First an overview was made of different absorption features in hyperspectral data of the observed minerals from literature and from this study (Abderrazak et al., 2018; Bishop et al., 2008; Bowitz & Ehling, 2008; Cloutis et al., 2002; Guinness et al., 2007; Kokaly et al., 2017). For reference, a dotplot was made of the developed decision trees (Fig. A.1.1). The “Beidellite(?)” group, which differs from the other groups in the decision tree, is discussed in section 4.2. This decision tree was applied to a combination of wavelength maps per sample and classified spectra as individual minerals. The different wavelength maps were also individually classified applying decision trees with classification in mineral groups (van Ruitenbeek, 2021).

2.4 Selection and processing of remote sensing data from Mars

Openly available data from Compact Reconnaissance Imaging Spectrometer for Mars (CRISM) onboard the Mars Reconnaissance Orbiter (MRO) were used to identify evidence of hydrothermal alteration in Martian impact craters. The Data Product Search of the Mars Orbital Data Explorer was used to acquire CRISM data of the selected Martian impact craters. The Martian craters were selected to fit into a crater size range of 20-42 km, have a variety of ages and topographical high resolution (sections 1.3.1 and 1.4.2).

The Map-Projected Targeted Reduced Data Record (MTRDR) data were used, as these are already corrected for I/F, geometric, photometric, atmospheric, and instrumental effects, are map projected, and bad band removal is applied. This is most similar to the processing steps that are applied to the processed hyperspectral data measured from the Brazilian analogues (Murchie et al., 2007; van Ruitenbeek, 2021). The MTRDR data consist of a hyperspectral image cube, spectral summary parameters, browse products, data processing information maps, a map projected version, and a table with the wavelength information (Murchie et al., 2007). The MTRDR data of Auki have a topographical resolution of 36 m/pixel and of the other selected craters of 18 m/pixel. The data consist of 489 bands, measured over a spectral range of 436.13-3896.76 nm, which corresponds to a hyperspectral resolution of ~7 nm.

Bands 436.13-1000 nm and 2500-3896.76 nm were removed using the “Subset/convert” tool in Hyppy3. The “Median 9+9+9 neighborhood” tool in the spectral median filter of Hyppy3 was used to smooth the CRISM data. The developed decision tree and decision tree for classifying mineral groups (van Ruitenbeek, 2021) were applied to the processed MTRDR data.

Finally, the amount and types of hydrothermal alteration were compared between mineral classifications of the Brazilian samples, classifications of the selected Martian craters in this study and classifications of the same craters in other studies (sections 3.4.2 and 4.4).

3. Results

Hydrothermal alteration is observed in two types of veins in the sample set, which are distinguished based on their white and red color, respectively. These veins occur throughout the sample set and are discussed below showing data from optical microscopy, BSE images, EDS data, mean spectra per hydrous mineral and mineral classification based on hyperspectral data. To allow for comparison with Martian impact craters, mineral classification based on data from the Brazilian sample set is followed by mineral classifications based on CRISM data.

3.1 Optical microscopy

3.1.1 White veins

In white veins a combination of zeolites, quartz, and clays is observed using optical microscopy (Fig. 3.1). The zeolite is characterized by its colorless to grey appearance in Plain Polarized Light (PPL), light to dark grey interference colors and straight extinction (Fig. 3.1). A color difference is observed within the white veins, indicating two types (Fig. 3.1.A/B). Quartz has a spotty, colorless appearance in PPL and white to light grey interference colors. In Crossed Polarized Light (XPL) it shows undulous extinction. Quartz can be located on the edge of the vein surrounding chabazite, but can also been seen as patches in between chabazite (Fig. 3.1.A). Veins consisting of only quartz are present in the sample set. A thin band of clays at the edge of the vein, surrounding quartz and/or zeolite is present in sample VG1B, VG2, VG8 and VG12. The clays are dark green in PPL (Fig. 3.1.C/D) and are further distinguished through EDS data (section 3.2.2).

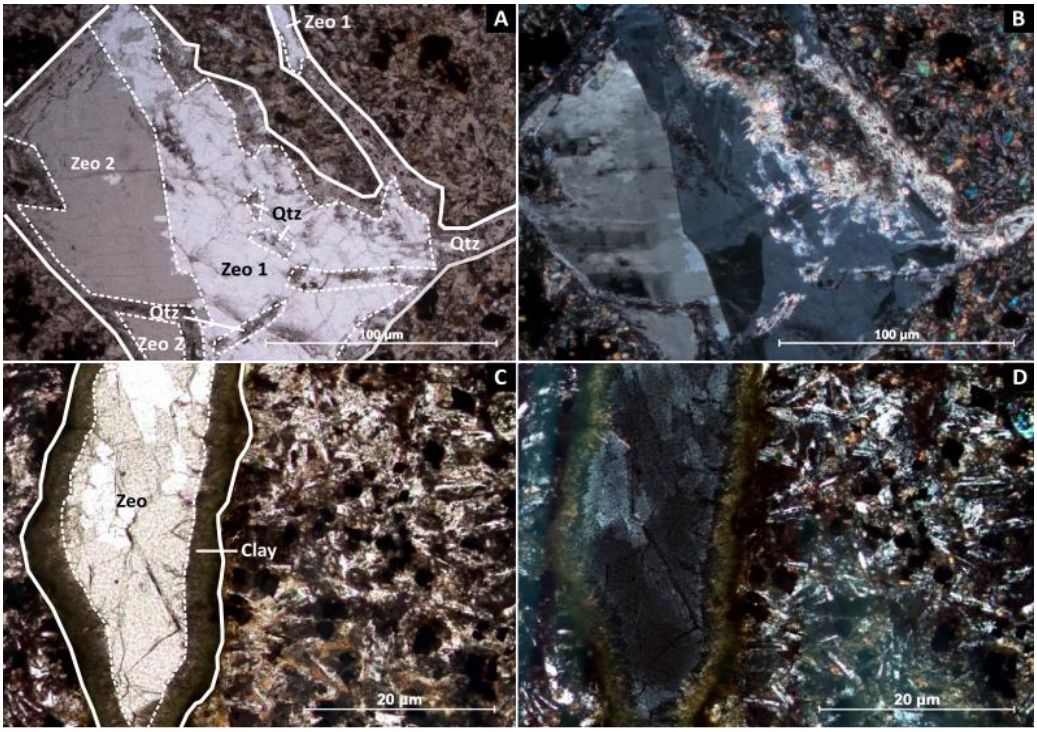

Fig. 3.1 White veins observed with optical microscopy and annotated using SEM data. White thick lines indicate the border between the vein to the matrix. Dotted lines show the estimated border between individual minerals. A. White vein in sample VG18, showing zeolite 1 and zeolite 2 with quartz on the edges of the vein and in between the zeolite in PPL. B. White vein in sample VG18 in XPL. C. White vein in sample VG8, showing zeolite with clays on the edges of the vein in PPL. D. White vein in sample VG8 in XPL.
Abr. Zeo – Zeolite, Qtz - Quartz

3.1.2 Red veins

The red veins show dark bands, containing oxides (Fig. 3.2). The light bands in between the dark bands consist of fragments (< 10 µm) of chabazite and quartz, which are also present in the white veins (Fig. 3.2). Furthermore, the lighter bands contain fragments (<10 µm) of plagioclase and pyroxenes, which are also located in the matrix surrounding the veins. The structure in the bands is chaotic and due to the high concentration of oxides the different fragments in red veins are badly visible using optical microscopy (Fig. 3.2). Oxides can be distinguished from their dark red-brown color in both PPL and XPL. Plagioclase is characterized by its colorless appearance in PPL, dark grey color and twinning in XPL, and a long prismatic shape, when not fragmented. Clinopyroxene is colorless in PPL, has high relief, yellow/blue/purple interference colors and an inclined extinction in XPL. Because of the small sizes, the fragments are further distinguished through EDS data (section 3.2.2).

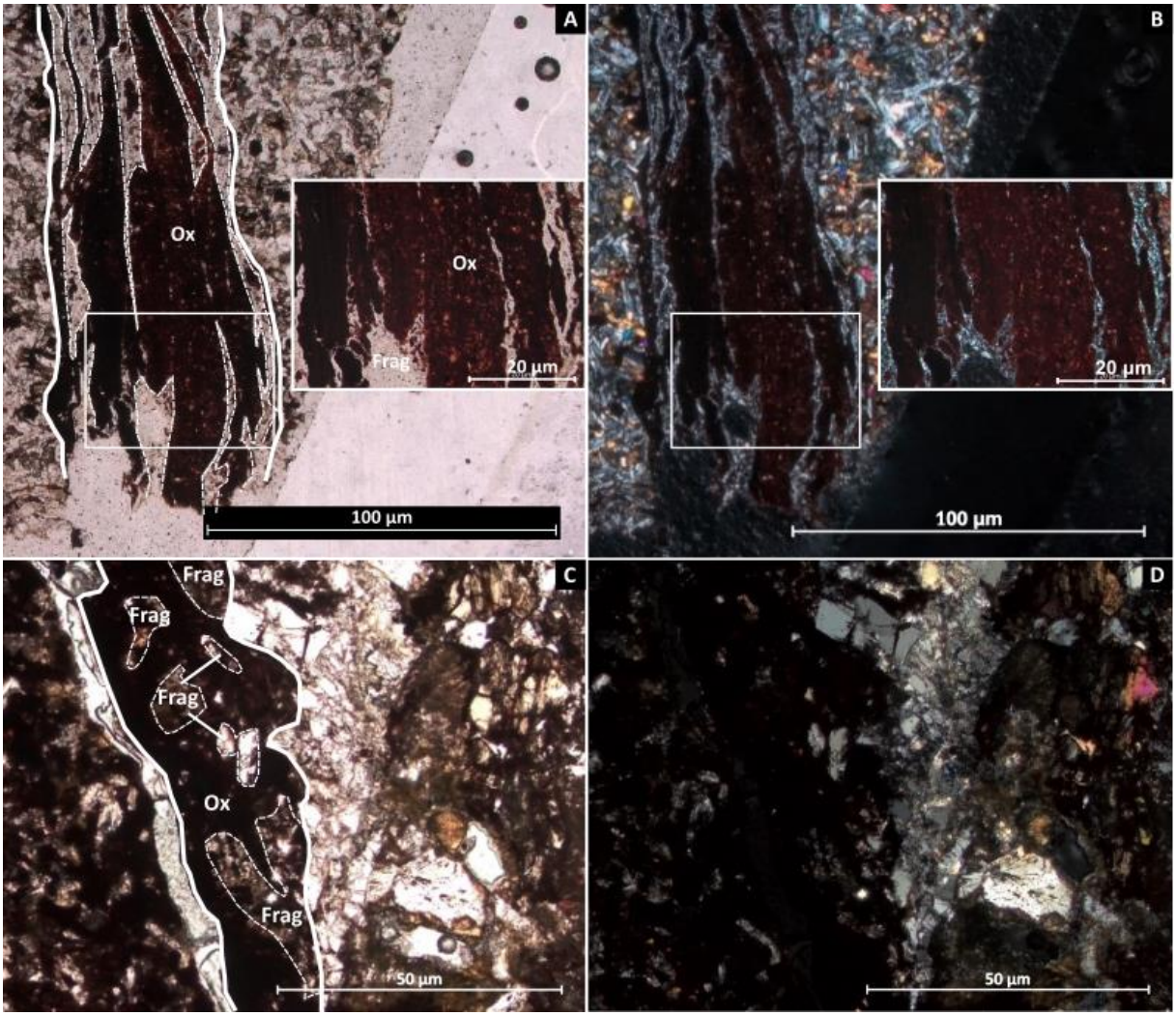

Fig. 3.2 Red veins observed with optical microscopy and annotated using SEM data. White thick lines indicate the border between the vein to the matrix. Dotted lines show the estimated border between individual minerals. A. Red vein in sample VG20, showing 10-50 µm dark bands with oxides and <10 µm fragments of zeolite, quartz, plagioclase and pyroxenes in PPL. B. Red vein in sample VG20 in XPL. C. Red vein in sample VG1B, showing big dark bands with oxides and small fragments

3.2 Scanning electron microscopy (SEM)

3.2.1 BSE images

White veins

White veins are distinguished from the matrix in Backscattered Electron (BSE) images through an increased homogeneity compared to the surrounding matrix (Fig. 3.3). The appearance of chabazite and heulandite from BSE images is similar, as these minerals are darker than calcite, clinopyroxene, and oxides and contain several fractures (Fig. 3.3.A). The BSE image of sample VG18 shows a fracture, which is observed through color difference using optical microscopy (Fig. 3.1). Quartz and zeolites are difficult to distinguish from each other from BSE images. Zeolites show more fractures compared to quartz and the texture of quartz is dotted and more chaotic compared to the relatively smooth zeolites (Fig. 3.3.B). Clays show a very typical chaotic needle-like texture with the sharp tips pointing to the core of the vein (Fig. 3.3.C). Furthermore, a second type of clay shows a more chaotic, flowy structure and darker color, when compared to the zeolite in the BSE image (Fig. 3.3.E). These differences could be explained by the presence of two different types of clay in the white veins. Calcite is illustrated on BSE images as light grey, smooth minerals with some transitions to darker/lighter grey colors (Fig. 3.3.D).

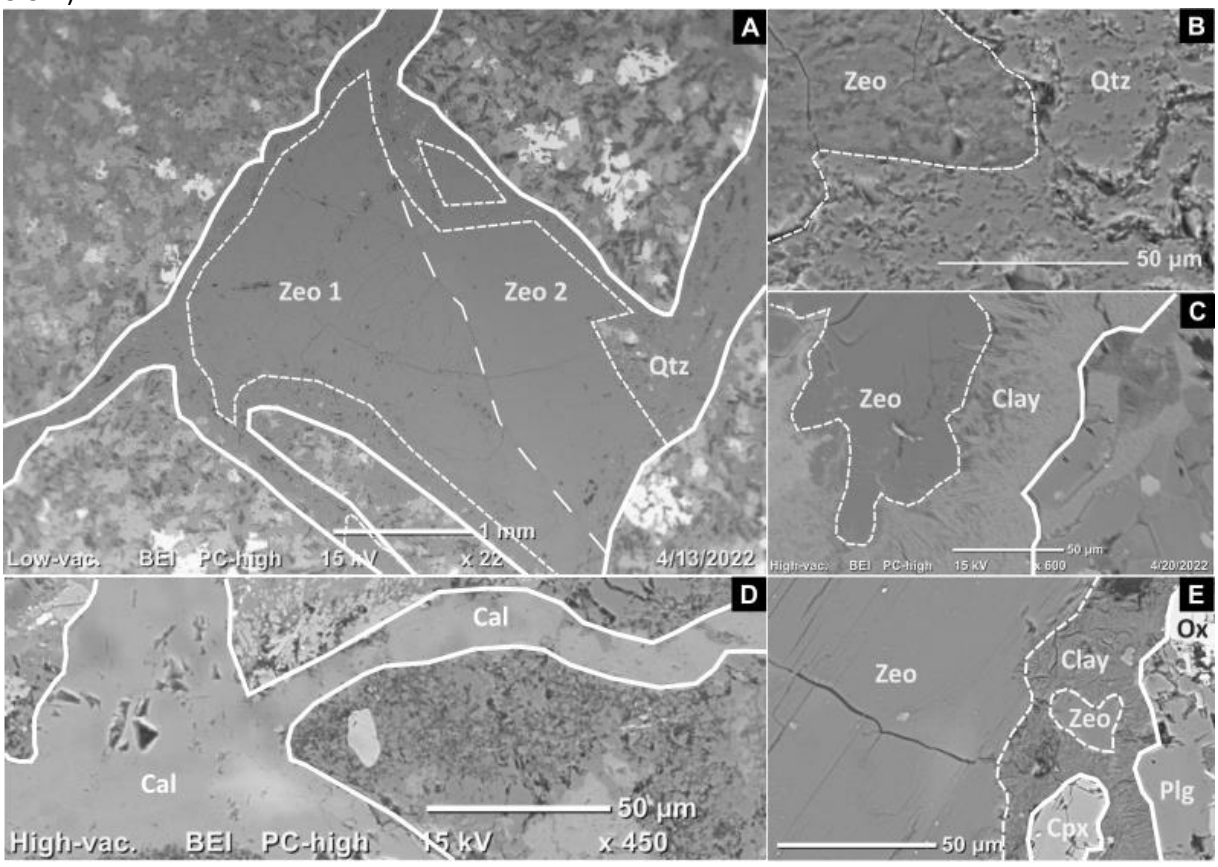

Fig. 3.3 Overview of the minerals present in white veins in BSE images. White thick lines indicate the border between the vein to the matrix. Dotted lines show the estimated border between individual minerals. A. Matrix and a white vein in VG18 showing two types of zeolites. B. The edge of a white vein in VG25 containing zeolite and quartz. C. Matrix and white vein in VG8 containing zeolite and clay. D. White vein in VA92 containing calcite. E. The edge of a white vein in VG12 containing zeolite and clay.

Abr. Zeo – Zeolite, Qtz – Quartz, Cal – Calcite

Red veins

Red veins can be recognized in BSE images by their relatively smooth and banded appearance and the smaller fragment sizes compared to the matrix (Fig. 3.4.A/C). Oxides can be recognized by their bright appearance in BSE images compared to other minerals (Fig. 3.4.B). In red veins most of the present oxides are very fragmented and cover around 30% of the vein. The oxides are surrounded by fragments of zeolites, quartz, plagioclase, pyroxenes, and kali feldspar (Fig. 3.4.B/D). The types of oxide cannot be determined from either BSE images or EDS data.

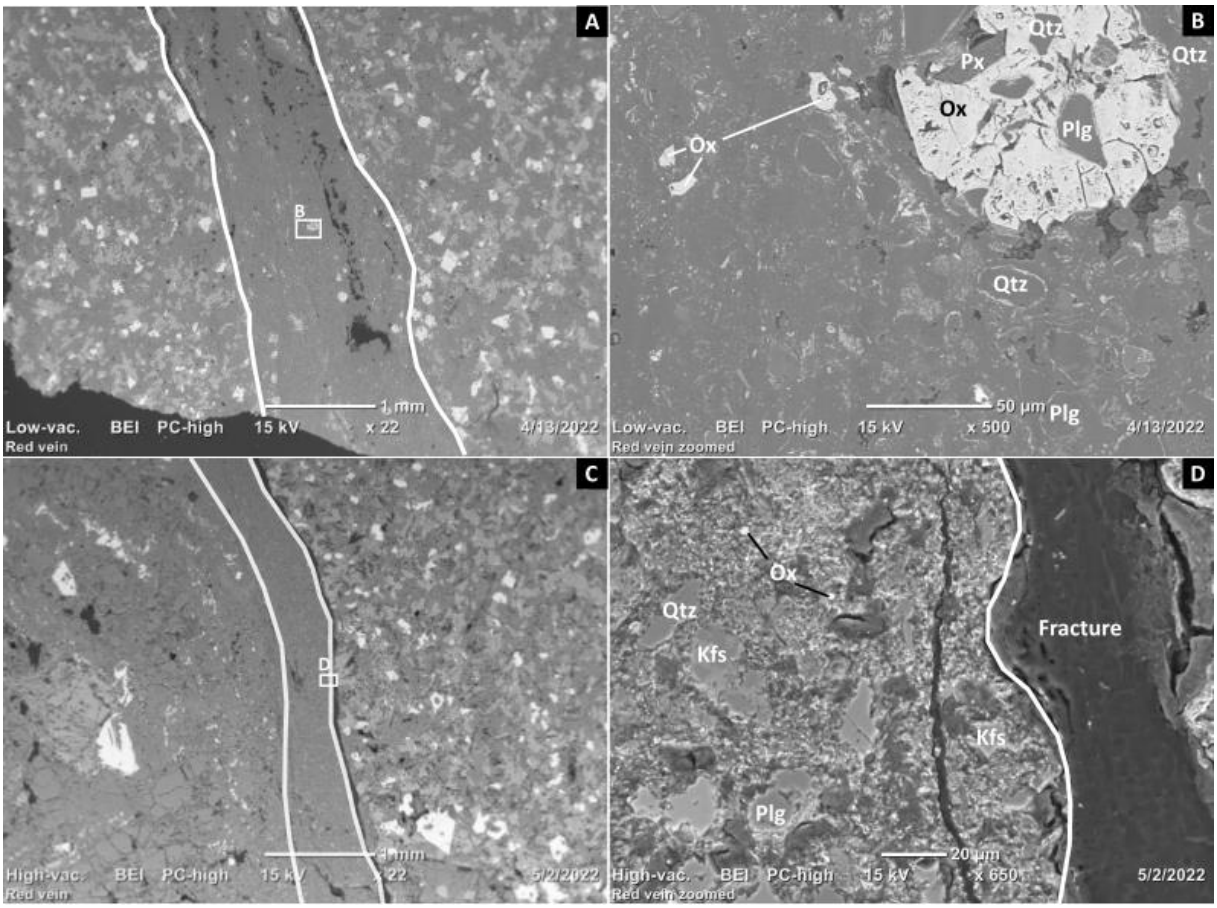

Fig. 3.4 Overview of the minerals present in red veins in BSE images. White thick lines indicate the border between the vein to the matrix. Dotted lines show the estimated border between individual minerals. A. Matrix and a red vein in VG20. B. Detail from VG20, illustrated by the rectangle in A, showing fragments surrounded by small patches of oxides and a big oxide. C. Matrix and red vein in VG1B. D. Detail from VG1B, illustrated by the rectangle in C, showing fragments surrounded by oxides in a chaotic structure and a big fracture on the right side of the vein.
Abr. Ox – Oxide, Qtz – Quartz, Plg – Plagioclase, Px – Pyroxene, Kfs – K-feldspar

3.2.2 EDS data

EDS data show different compositions for zeolites, quartz, clays, pyroxenes, plagioclase, (iron)oxides, and calcite, described in sections 3.1 and 3.2.1, and supplement and confirm the observations from optical microscopy (Table 3.1). With the composition of the zeolites no difference between zeolite 1 and zeolite 2 is observed (section 3.1.1). Two different compositions of clays are distinguished, which could point to the presence of two types of clays (Table. 3.1).

Table 3.1 Average compositions of different minerals in % from EDS data, observed throughout different thin sections of the selected samples.
** Number of locations on which the average composition of the mineral is based.*

Type	**Zeolite 1**	**Zeolite 2**	**Clay 1**	**Clay 2**
n*	21	3	11	9
N	-	-	3.9	2.7
SiO_2	66.8	68.1	55.8	52.2
Al_2O_3	21.5	20.9	5.9	11.0
MgO	-	-	8.0	21.7
CaO	9.2	8.8	0.6	2.0
Na_2O	0.1	0.6	-	-
K_2O	2.3	1.6	5.1	0.8
FeO	-	-	20.7	9.7
Possible minerals	Chabazite	Heulandite	Celadonite	Beidellite

3.3 Characteristic mineral spectra from SWIR data

Characteristic spectra of the main four alteration minerals (Table 3.1 and section 3.4) and the matrix are shown in Fig. 3.5. Table 3.2 shows the wavelength positions of the observed absorption features in the mean characteristic spectra. The absorption features in the spectrum of zeolite 2 are similar to those of zeolite 1 and do not enable distinguishing between different zeolites when only hyperspectral data are used (Fig. 3.5).

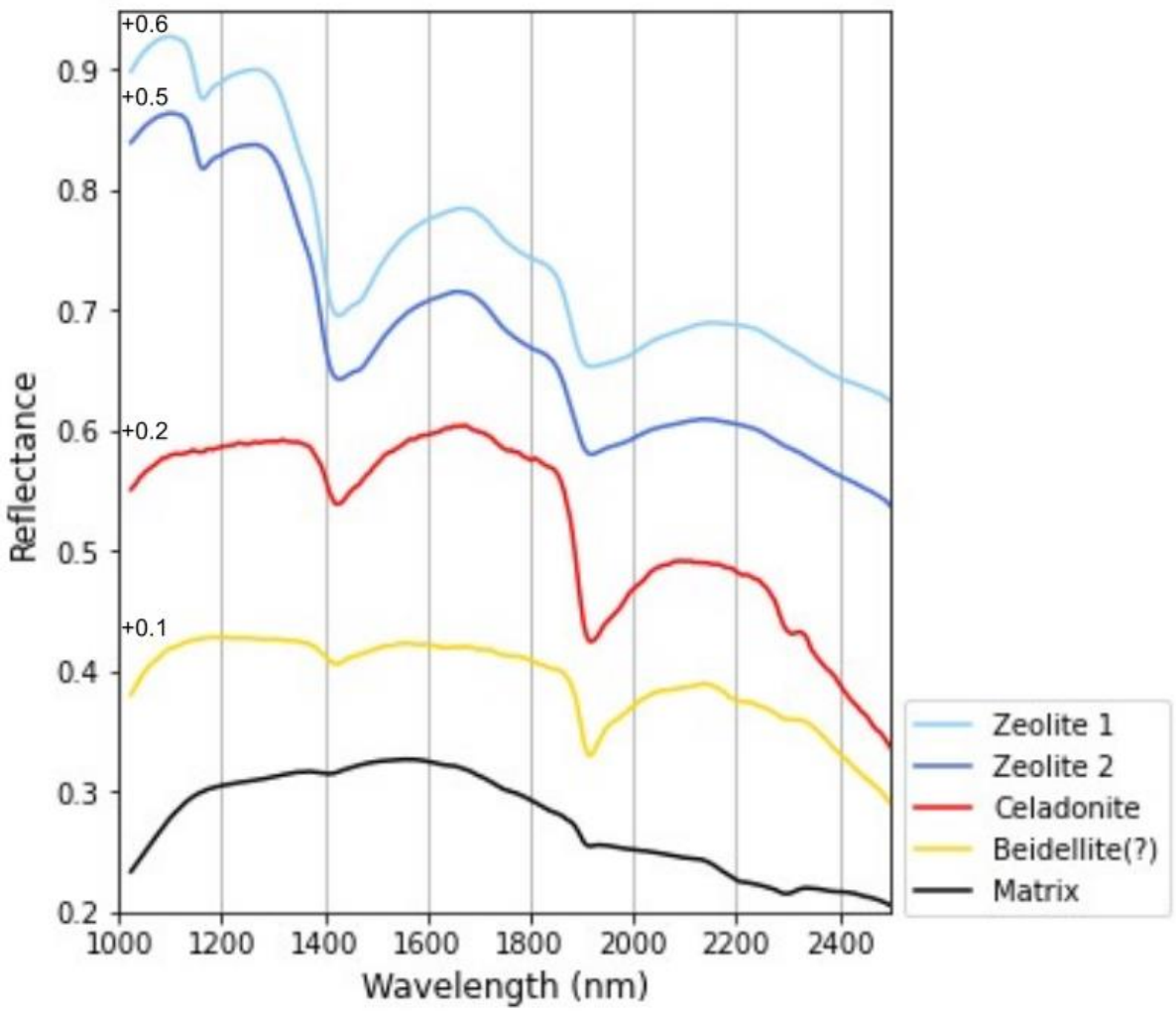

Fig. 3.5 Characteristic mean spectra of hydrothermal minerals, zeolite 1, zeolite 2, celadonite, beidellite(?) and the matrix. +… shows the shift in reflectance per hydrothermal mineral that is necessary to separately display all spectra. Table 3.2 shows the precise wavelength position of the present absorption features per hydrothermal mineral and matrix.

Table 3.2 Wavelength position of observed absorption features in the mean characteristic spectra in figure 3.5 for zeolite 1, zeolite 2, celadonite, beidellite(?) and the basaltic matrix.

Feature	Sample	Mean wavelength position of absorption features (nm)
Zeolite 1	VG25	1165, 1427, 1470, 1920
Zeolite 2	VG18	1165, 1429, 1470, 1920
Celadonite	VG8	1426, 1917, 2213, 2308
Beidellite(?)	VG12	1425, 1915
Matrix	VG20	1409, 1915, 2296

3.4 Classification of hydrothermal alteration based on SWIR data

3.4.1 Samples from Vista Alegre and Vargeão

After applying the developed decision tree for the classification of hydrothermal minerals, section 2.3.2, to the spectroscopic images of the selected thin sections the minerals in the veins are visualized (Fig. 3.6.A.I and 3.6.B.I and A.1.2.A-G.I). Especially the zeolites are well visible, but an obvious division between zeolite 1 and zeolite 2 is not visible (Fig. 3.6.A.I and section 4.1). Celadonite is also well-distinguished and is present throughout the veins of VG8 and at the edges of the veins of VG2 (Fig. 3.6.B.I and A.1.2.B.I). This corresponds to the locations of clays from optical microscopy and SEM data (sections 3.1 and 3.2), with exception of VG12, where beidellite(?) is classified (sections 4.2 and 4.3.1). The matrix between the veins is classified as "Other" (Fig. 3.6.A/B.I and A.1.2.A-G.I), as basaltic minerals like amphibole, pyroxenes, olivines, and ilmenite, are not included in the developed decision tree.

For comparison other decision trees (van Ruitenbeek, 2021) were applied to the hyperspectral data (Fig. 3.6.A.II-VI, 3.6.B.II-VI and A.1.2.A-G.II-VI). In most samples, features classified by the developed decision tree are also visualized using these other decision trees (van Ruitenbeek, 2021). Classification in zeolites, chabazite, and heulandite is mostly present at the same locations as classification in groups B2, B3, D1, and E1 (Fig. 3.6.A and A.1.2.A/B/C/E). The locations of the classified celadonite correspond to the mineral groups B3, D1 and F12 (Fig. 3.6.B and A.1.2.B). Beidellite(?) is classified at the same locations as groups B3, D1, and F1 (Fig. 3.6.A. and A.1.2.C/F/G). The matrix is classified in group D1, D3, E2, F3, chlorite, and aspectral (Fig. 3.6. and A.1.2). Other features are only visible in the results using decision trees characterizing mineral groups, such as red veins and calcite (Fig. A.1.2.D and A.1.2.F and section 4.3.2).

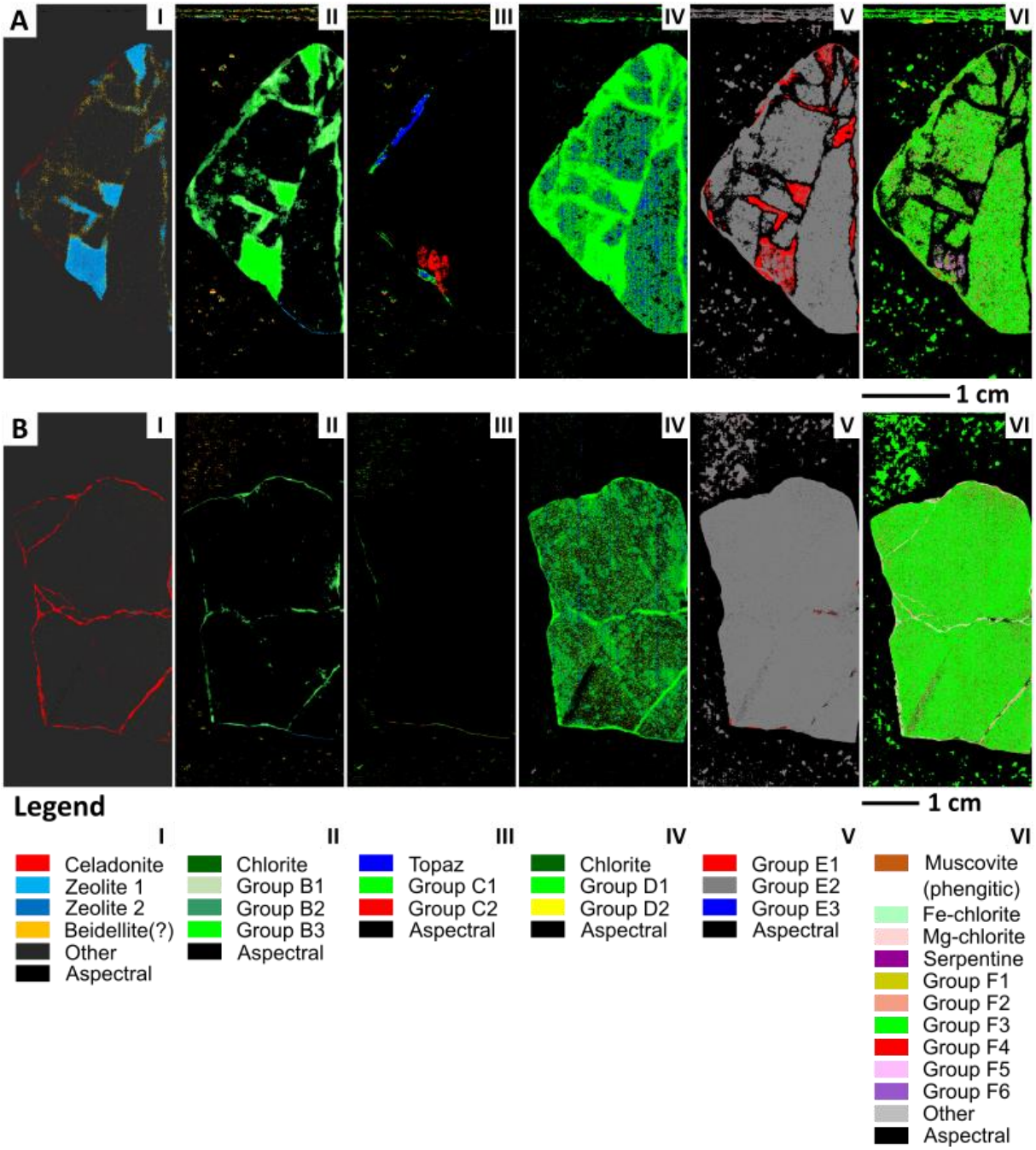

Fig. 3.6 A. Mineral classification of sample VG18. B. Mineral classification of sample VG8. I. Application of "Decision_tree_hydrothermal.tree" II. Application of van Ruitenbeek (2021) decision tree for images with a wavelength range of 1300-1600 nm III. of 1650-1850 nm. IV. of 1850-2100 nm. V. of 2000-2500 nm. VI. of 2100-2400 nm. (van Ruitenbeek, 2021).
The legend only includes the minerals that are classified in these hyperspectral images. A complete legend and content of the groups is present in Fig. A.1.3 and table A.2.3.

3.4.2 CRISM data

Most of the data from Martian craters do not have clear absorption features and are classified as aspectral (Fig. 3.7 and A.1.4). The developed decision tree classifies only few pixels as individual minerals in the center of Toro crater: illite, celadonite, and beidellite(?) (section 4.2), while most pixels are classified as "Other" (Fig. 3.7.A.I). The other decision trees (van Ruitenbeek, 2021) result into classifications of the center of Toro crater in D1, E3, F5, F6, F13, and prehnite (Fig. 3.7.A.IV-VI). The classification in individual minerals of Auki crater shows some clusters of chlorite and a few pixels of dickite/nacrite, glauconite and beidellite(?) (Fig. 3.7.B.I). Furthermore, a few pixels are classified as "Other", but these are not connected throughout the crater and are interrupted by aspectral pixels (Fig. 3.7.B.I). Only a few pixels are classified as chlorite, D1, D2, D3, E3, F3, F6, F7, F9, and F13 after applying the other decision trees in Auki crater (van Ruitenbeek, 2021) (Fig. 3.7.B.IV-VI). Canso crater lacks clear signals to indicate the presence of hydrous minerals (Fig. A.1.4.A). Laylà crater shows a very spotty classification in "Other" in the individual mineral classification (Fig. A.1.4.B.I) and in groups D2 and E3 after applying other decision trees (van Ruitenbeek, 2021) (Fig. A.1.4.B.IV/V).

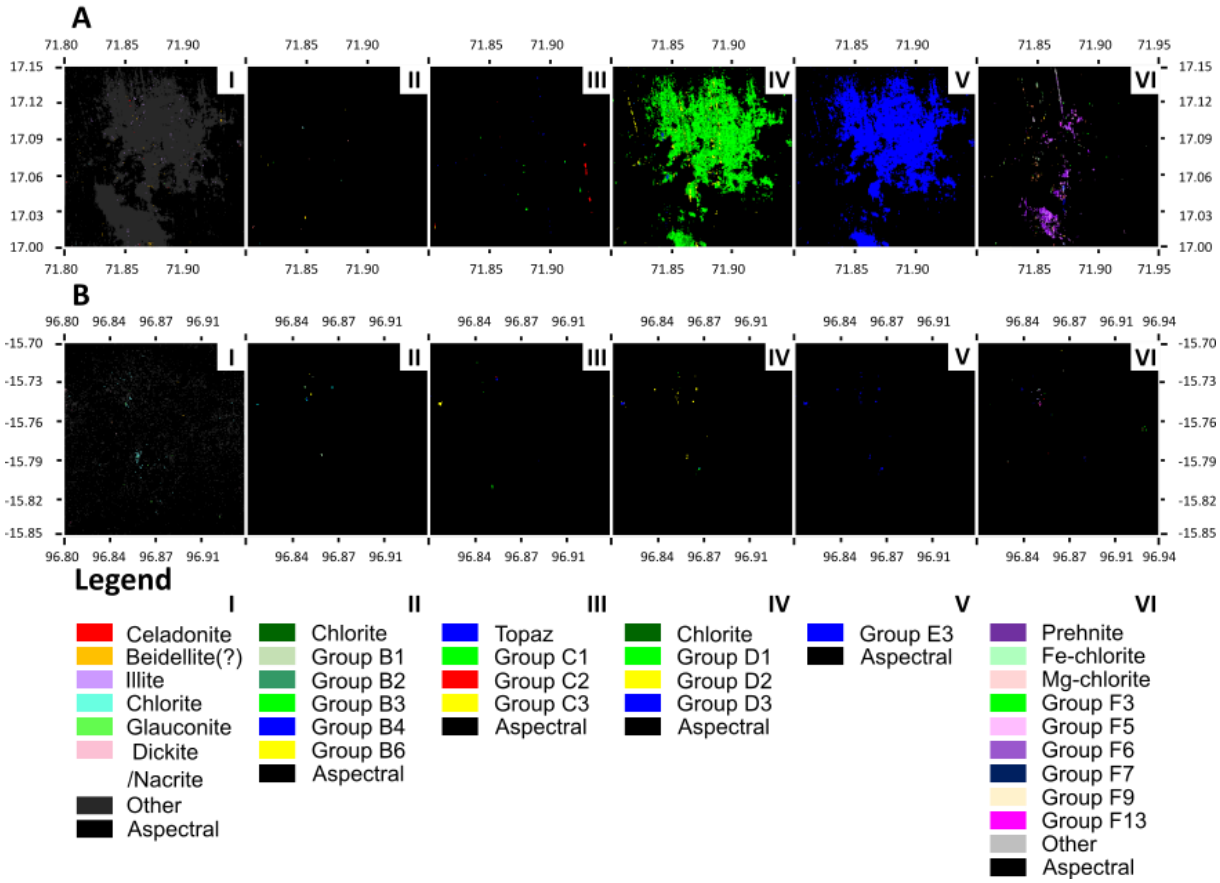

Fig. 3.7 A. Mineral classification of Toro crater. B. Mineral classification of Auki crater. I. Application of "Decision_tree_hydrothermal.tree" II. Application of van Ruitenbeek (2021) decision tree for images with a wavelength range of 1300-1600 nm III. of 1650-1850 nm. IV. of 1850-2100 nm. V. of 2000-2500 nm. VI. of 2100-2400 nm. (van Ruitenbeek, 2021).
The legend only includes the minerals that are classified in these hyperspectral images. A complete legend and content of the groups is present in Fig. A.1.3 and table A.2.3.

4. Discussion

Optical microscopy, BSE images and EDS data have shown the presence of zeolites, quartz, and clays within white veins and fragmented oxides, zeolites, quartz, plagioclase, pyroxenes, and kali feldspar within red veins (sections 3.1 and 3.2). White and red veins are distinguished from the matrix after classifying hyperspectral images with decision trees. Celadonite, zeolites, and beidellite(?) are distinguished in white veins, when classified into individual minerals (section 3.4.1). Red veins cannot be distinguished from the classification in individual minerals, but can be in classifications into mineral groups (section 3.4.1). Group D1 and F2 are mostly present in the red veins and groups B3, D1, and E1 in white veins (section 3.4.1). Martian impact crater Toro shows most hydrous minerals, of which a small part is distinguished as illite, celadonite, beidellite(?) and are mostly part of group "Other", D1, E3, F5, F6, F13, and chlorite (section 3.4.2).

4.1 Identification of the two main zeolites

The color difference using optical microscopy suggests two types of zeolites, but EDS data cannot indicate the different types (section 3.2.2). Raman data indicate the presence of chabazite and heulandite in the veins and therefore suggests that these are the two types of zeolites that occur in the samples (Alsemgeest et al., unpublished). Raman data show a dominant presence of chabazite, which is similar to the observation of dominant presence of zeolite 1 in optical microscopy images (Alsemgeest et al., unpublished).

4.2 Validation of mean characteristic mineral spectra

To validate the mean characteristic mineral spectra the absorption features observed in these spectra are compared with those from the literature. Overall, there is a good correspondence between wavelength positions of absorption features from the literature and from the mean characteristic mineral spectra, with exception of the absorption features at 970 nm for heulandite, at 2350 nm and 2480 nm for celadonite, at 2180 nm for beidellite(?), and at 2250 nm and 2340 nm for the basaltic matrix (Table 4.1)

The absorption feature at 970 nm for heulandite shows a significant bigger dip in reflectance than for chabazite, as observed in (Cloutis et al., 2002; Kokaly et al., 2017). The 970 nm absorption feature is not present in the mean characteristic spectra, as the wavelength range of the hyperspectral data is 1000-2500 nm (Table 4.1). The possibility to distinguish between chabazite and heulandite using hyperspectral data is discussed in section 4.3.1.

The observed absorption features in the calculated mean spectrum of celadonite are roughly similar to those observed in spectra from literature, with exception of the small absorption features at 2350 nm and 2480 nm that are present in the literature, but not in the measured spectra (Fig. 3.5 and Table 4.1) (Bishop et al., 2008). The dip in reflectance of these two features could be too low to classify using the developed decision tree. Furthermore, the lack of literature data on the characteristic spectrum of celadonite could cause inaccuracies in the presence of absorption features (Bishop et al., 2008).

The absorption feature at 2180 nm, as observed in spectra of beidellite from the literature, is not observed in the mean characteristic spectrum of beidellite(?) (Fig. 3.5 and Table 4.1) (Kokaly et al., 2017). This questions whether beidellite is classified by the developed decision tree or whether this group includes all hydrous minerals with absorption features around 1400 nm and 1900 nm, such as celadonite, illite, nontronite, kaolinite, halloysite, chabazite, heulandite, etc. (Fig. 3.5.D and A.1.1, and Table 4.1) (Kokaly et al., 2017). Therefore, this group is annotated as "Beidellite(?)", as hydrous minerals other than beidellite can be classified in this group.

The absorption features at 2250 nm and 2340 nm, as observed in (Zhou & Wang, 2017) for basalt is not observed in the mean characteristic spectrum of basalt (Table. 4.1). These features are characteristic for the presence of Al-OH and Mg-OH and are expected in weathered basalt spectra, as basalt contains Al and Mg (Zhou & Wang, 2017). The 2296 nm feature in the mean characteristic

spectrum of basalt does not correspond to the features observed in the literature (Table 4.1). This feature is also characteristic for the presence of Al-OH and Mg-OH and can therefore be explained by weathering of basalt. A different degree of weathering between the Devonian basalts in (Zhou & Wang, 2017) and the Cretaceous basalts in the Paraná basin could explain the difference in wavelength position of the absorption features.

Table 4.1 Comparison between the absorption features per mineral observed in literature, the range of absorption features used in the developed decision tree and the absorption features observed in mean characteristic spectra (section 3.3). "n.a." indicates that the absorption feature observed in the literature is not used in the decision tree to classify the mineral. "×" indicates that the absorption feature observed in the literature is not observed in the calculated mean characteristic spectra. (Bishop et al., 2008; Cloutis et al., 2002; Kokaly et al., 2017; Zhou & Wang, 2017).

Mineral	Absorption feature in literature	Absorption feature range in decision tree	Absorption feature in mean characteristic spectra
Chabazite	1160 nm	1140 nm – 1180 nm	1165 nm
	1430 nm	1400 nm – 1450 nm	1427 nm
	1470 nm	n.a.	1465 nm
	1915 nm	1900 nm – 1950 nm	1920 nm
Heulandite	970 nm	<1050 nm	×
	1160 nm	1140 nm – 1180 nm	1165 nm
	1430 nm	1400 nm – 1450 nm	1429 nm
	1470 nm	n.a.	1465 nm
	1915 nm	1900 nm – 1950 nm	1920 nm
Celadonite	1410 nm	1400 nm – 1450 nm	1426 nm
	1920 nm	1900 nm – 1950 nm	1917 nm
	2205 nm	n.a.	2213 nm
	2305 nm	2290 nm – 2310 nm	2308 nm
	2350 nm	2340 nm – 2380 nm	×
	2480 nm	n.a.	×
Beidellite(?)	1410 nm	1400 nm – 1450 nm	1425 nm
	1910 nm	1900 nm – 1950 nm	1915 nm
	2180 nm	2160 nm – 2200 nm	×
Basalt	1410 nm	n.a.	1409 nm
	1915 nm	n.a.	1915 nm
	2250 nm	n.a.	×
		n.a.	2296 nm
	2340 nm	n.a.	×

4.3 Reliability of the developed decision tree

Individual minerals were classified from hyperspectral data using the developed decision tree. Furthermore, decision trees classifying the hyperspectral data into mineral groups have been applied (van Ruitenbeek, 2021). Overall, there is a good match between the classification of the hyperspectral data using the developed decision tree and the optical microscopy and SEM data and the classification based on other decision trees. Below the differences between the classification of hyperspectral data using the developed and other decision trees, and optical microscopy and SEM data are discussed.

4.3.1 Comparison of the classification images with optical microscopy and SEM data

In the developed decision tree the distinction between chabazite and heulandite was tested by using the absorption feature below 1050 nm to classify heulandite (Fig. A.1.1). Heulandite has an absorption feature at 970 nm, which is not present in the wavelength range of 1000-2500 nm of the hyperspectral data (Table 4.1). The absorption feature at 970 nm in the characteristic spectrum of heulandite results in a decrease of the reflectance below 1050 nm. This characteristic is used to distinguish between

chabazite and heulandite. It was tested whether this decrease towards the absorption feature at 970 nm would be classified as an absorption feature. The developed decision tree would then classify heulandite, when the 3rd deepest absorption feature in the range 1000-1500 nm is below 1050 nm. The locations where heulandite is present, are not connected and very randomly scattered. Furthermore, the classified location does not correspond to the location of zeolite 2, heulandite, in VG18 observed with optical microscopy (Fig. 3.1 and 3.6.A.I). So using the measured hyperspectral data no distinction can be made between chabazite and heulandite. In the classification of VG28B using the developed decision tree no chabazite or heulandite is distinguished, whereas this would be expected from optical microscopy and SEM data (Fig. A.1.2.F.I and Table A.2.2). It is unclear why the unclassified data of VG28B lacks a clear absorption feature around 1160 nm.
In the classification of VG1A, VG2, VG20, VG28B, and VA92 celadonite is scattered throughout the image (Fig. A.1.2.A/B/D/F/G.I), while this is not observed in optical microscopy and SEM data (sections 3.1 and 3.2). This could be due to the similar spectra of celadonite and the basaltic matrix (table 4.1) or the lack of optical microscopy and SEM data of the matrix. When the absorption feature at 2350 nm of celadonite is unclear, basalt could be classified instead of celadonite, and explain the scattered celadonite pixels throughout the matrix (Fig. A.1.1).
In VG18 beidellite(?) has been classified on the edge of the white veins, while no clays have been observed using optical microscopy and EDS data (Fig. 3.6.A.I and Table A.2.2). This questions the classification of only beidellite by the developed decision tree. As this group also includes all hydrous minerals with absorption features around 1400 nm and 1900 nm (section 4.2), the classification does not conflict with the optical microscopy and EDS data. Beidellite(?) is classified in the lower right part of the thin section from VG28B and throughout the complete thin section of VA92 (Fig. A.1.2.F/G.I), while this does not correspond to the optical microscopy and SEM data, as no clays are observed at these locations. In VG28B a dichotomy is observed in the thin section using optical microscopy, where one side of the matrix has bigger crystal sizes and a lower degree of oxidation compared to the other side. As the beidellite(?) is located near the edge of the thin section in VG28B and does not match with one part of the observed dichotomy, it is expected that the classification is caused by a lower data quality in the hyperspectral data near the edge of the thin section (Pillay et al., 2020). From optical images of the very weathered sample VG92 it is unclear whether clays are present within the matrix. BSE images and EDS data have not indicated the presence of clay within veins and the matrix. The low amount of SEM data cannot exclude the presence of clays in VA92. The reliability of the classification in beidellite(?) is also questioned by the scattered classified pixels on the edges of the white veins. This could be because of the very thin clay layer at the edge of the vein, which could cause less clear reflectance signals of beidellite. More data is necessary to exclude the presence of beidellite in VG12, VG18, VG 28B, and VA92.
No calcite has been classified in VA92 using the developed decision tree, while this is observed using optical microscope and EDS data (Fig. A.1.2.G.I and Table A.2.2). This questions the clearness of the absorption features used in the decision tree and the applicability of the decision tree to classify calcite.

Oxides and minerals in basalt do not have exclusive absorption features and could not be added to the developed decision tree. Therefore, the red veins in VG2 and VG20 and matrix are not visualized by the classification in individual minerals (Fig. A.1.2.B/D) and are classified as “Other”.

4.3.2 Comparison of the classification images between application of the developed decision tree and other decision trees

Classification in group B3 and E1 at the same location as zeolites is not expected from the present minerals in these groups, as zeolites are not included (Table A.2.3). In the spectra of zeolites from the literature no absorption feature is present in the wavelength range from 2000-2500 nm and why group E1 is classified at matching positions with zeolites is therefore unclear (Fig. 3.5.A/B) (van Ruitenbeek, 2021). Classification in B3 can be caused by the 1465 nm feature, a relatively small dip in reflectance (Table 4.1). Preference is given to the developed decision tree to classify chabazite and heulandite, as

this is based on the absorption feature around 1160 nm that shows a bigger dip in reflectance (Fig. 3.5.A/B and Table 4.1).
Celadonite and beidellite are not incorporated in the classifications into mineral groups, which makes direct comparison with the results of the developed decision tree impossible. Celadonite does not meet the requirements to be classified in group B3 and therefore it is unclear how these are classified at the same locations (Fig. 3.6.B and A.1.2.B). The veins in VG8 are more continuously classified as celadonite using the developed decision tree, while these veins are less continuously classified as different groups using the decision trees of van Ruitenbeek (2021) (Fig. 3.6.B). Therefore, preference is given to the developed decision tree to classify celadonite.
Classification of beidellite(?) into B3 is a result of the structure of the decision tree for the wavelength range 1300-1600 nm and does not fit with the spectrum of beidellite, because no absorption feature is present between 1500 nm and 1600 nm (Fig. 3.6.A.II and A.1.2.C/F/G.II) (van Ruitenbeek, 2021). Inaccuracies in the wavelength position of the absorption feature around 2180 nm of beidellite could explain the same locations for classification of group F1 and beidellite(?) (Fig. A.1.2.F.VI) (van Ruitenbeek, 2021).
No calcite has been classified in VA92 using the developed decision tree (Fig. A.1.2.G.I). However, in the mineral group classification of the 2100-2400 nm image group F5, containing calcite, has been distinguished (Fig. A.1.2.G.VI). A weak signal of the 2nd deepest absorption feature in the 2100-2400 nm range of calcite could explain the absence of calcite in the classification, when the developed decision tree is applied. Therefore, preference is given to the classification in mineral groups to classify calcite. This cannot be used solely, as also other minerals are present in F5 and without additional optical and scanning microscopy the presence of calcite cannot be confirmed.

The red veins in VG2 and VG20 are not visualized by the classification in individual minerals, but can be distinguished by classifications in mineral groups (Fig. A.1.2.B/D.IV/VI). The difference between the red vein and the matrix is the absence of group D3 in the red vein (Fig. A.1.2.B/D.IV). It is unclear why the wavelength position of the deepest absorption feature has a bigger range in the matrix than in the red vein. F2 and (phengitic) muscovite are present at a higher concentration in the red vein of VG20 compared to the matrix (Fig. A.1.2.D.VI), which is not in line with observations from optical and backscattered electron microscopy (sections 3.1.2 and 3.2). Basalt and oxides do not show clear absorption features around the wavelength positions used to classify F2 and muscovite (Kokaly et al., 2017). The higher concentration of these two hydrated phyllosilicates in red veins could be a 2nd generation of hydrothermal alteration, as the combination of illite and muscovite is not similar to the hydrous minerals observed in the white veins (section 4.6.1). Overall, the red veins are best visualized using the decision trees classifying in mineral groups and therefore preference is given to these classifications to distinguish red veins.

The classification of the matrix in chlorite, when using other decision trees (van Ruitenbeek, 2021), does not match with the classification by the developed decision tree and with optical microscopy and SEM data (Fig. 3.6.A/B.IV and A.1.2.A-G.IV). Chlorite is classified in 1850-2100 nm decision tree based on a 2nd deepest absorption feature in between 1950 nm and 1990 nm (van Ruitenbeek, 2021). This does not correspond with the calculated mean spectrum of basalt and therefore it is unclear why some pixels in the matrix are classified as chlorite (Fig. 3.5.E). A broad water feature around 1900 nm could explain the classification of the matrix in chlorite (Table. 4.1).

In future work, the developed decision tree can be applied in combination with other decision trees (van Ruitenbeek, 2021) to terrestrial samples to provide an accurate estimate of not only the present mineral groups, but also of individual minerals in a sample, which adds to a complete overview of the mineral content.

4.4 Mineral identification of Mars

The classifications of Mars using the developed decision tree differ from classifications in other studies. Craters Canso and Laylá lack clear signals in the classifications. Below the mineral identification on Mars by the developed and other decision trees is discussed and compared with mineral identification in Brazilian samples.

4.4.1 Toro crater

For validation of the application of the developed decision tree to CRISM data, the classifications of Toro crater using the developed and other decision trees are compared with the results of Marzo et al. (2010) (Fig. 4.1). The developed and other decision trees have classified the following minerals and mineral groups in the center of Toro crater: illite, celadonite, beidellite(?), “Other”, D1, E3, F5, F6, F13 and prehnite (section 3.4.2 and table A.2.3). Using spectroscopic observations hydrated silicate deposits, including prehnite, chlorites, smectites, and opaline materials are identified by Marzo et al. (2010). Classification in F5, F6, and F13 (table A.2.3) includes different phyllosilicates and could therefore correspond to the phyllosilicates observed in the study of Marzo et al. (2010). Illite is classified in a few pixels in the individual mineral classification, but is not observed from the spectroscopic classification in (Marzo et al., 2010). In Marzo et al. (2010) a combination of absorption features around ~1920, 1410 nm and 2220 nm results in classification of Al-smectite or opal material, while the developed decision tree classifies this combination of absorption features as illite (Fig. A.1.1). This explains the absence of illite in Marzo et al. (2010). The locations of classified illite by the developed decision tree are not continuous, but scattered throughout the image, which questions the presence of illite (Fig. 4.1.A). The classification using the developed decision tree has the best match with hydrous minerals observed in Marzo et al. (2010), but can only classify a limited amount of individual minerals. The developed decision tree could be too detailed to apply to Martian data that contain a lot of noise (section 4.5). The classification in the range of 2100-2400 nm of van Ruitenbeek (2021) is able to distinguish between locations with or without smectite and is able to classify prehnite. However, this decision tree cannot classify all the different groups that are distinguished in Marzo et al. (2010) (Fig. 4.1). A classification based on mineral groups and individual minerals that is designed especially for application on Mars should result in the highest detail, as the majority of pixels are classified as “Other” and cannot be distinguished individually with the applied processing steps.

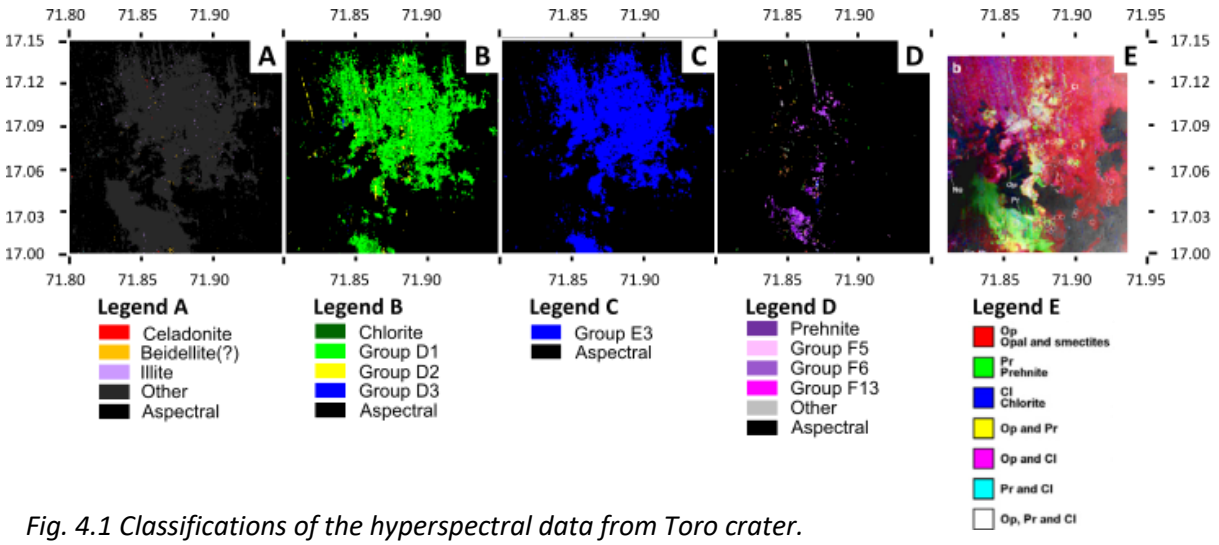

Fig. 4.1 Classifications of the hyperspectral data from Toro crater.
A. Application of "Decision_tree_hydrothermal.tree". B. Application of van Ruitenbeek (2021) decision tree for images with a wavelength range of 1850-2100 nm. C. Application of van Ruitenbeek (2021) decision tree for images with a wavelength range of 2000-2500 nm. D. Application of van Ruitenbeek (2021) decision tree for images with a wavelength range of 2100-2400 nm. E. Classification of the Toro crater in (Marzo et al., 2010). Legends A-D only include the minerals that are classified in these hyperspectral images. A complete legend and content of the groups is present in Fig. A.1.3 and table A.2.3. Legend E of 4.3.E (Marzo et al., 2010).

4.4.2 Auki crater

The classification of Auki crater in hydrous minerals in Carrozzo et al. (2017) is very different from the classifications shown in this study. In Carrozzo et al. (2017) mostly opaline silica and phyllosilicates are classified in the central ring of Auki crater and a minor amount in carbonates/chlorites, zeolites, and serpentines (Fig. 4.2). The presence of chlorite does not correspond well to the locations where F6 and F13 are classified and to the amount of chlorite classified in Carrozzo et al. (2017) (Fig. 4.2). The discontinuous nature of the classifications after applying the different decision trees and the misfits between the individual minerals and the groups questions the quality of these classifications. Furthermore, the absence of signals for carbonates, zeolites, and serpentines that are observed in Carrozzo et al. (2017) could indicate a low quality of the classification after applying the different decision trees (sections 4.5 and 4.6).

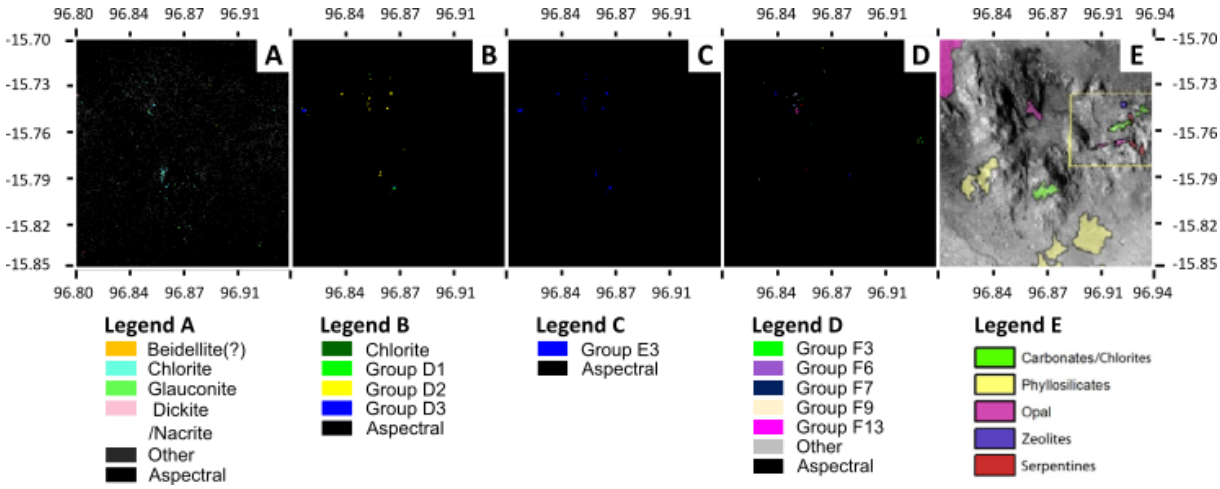

Fig. 4.2 Classifications of the hyperspectral data from Auki crater.
A. Application of "Decision_tree_hydrothermal.tree". B. Application of van Ruitenbeek (2021) decision tree for images with a wavelength range of 1850-2100 nm. C. Application of van Ruitenbeek (2021) decision tree for images with a wavelength range of 2000-2500 nm. D. Application of van Ruitenbeek (2021) decision tree for images with a wavelength range of 2100-2400 nm. E. Classification of the Auki crater in Carrozzo et al. (2017). Legends A-D only include the minerals that are classified in these hyperspectral images. A complete legend and content of the groups is present in Fig. A.1.3 and table A.2.3. Legend E of 4.2.E (Carrozzo et al., 2017).

4.4.3 Nili Fossae

The study of (van Ruitenbeek et al., 2014) is compared with this study to further indicate the applicability of the developed decision tree to CRISM data. The Nili Fossae area on Mars is known for its great diversity of hydrous minerals (Ehlmann et al., 2009). In the study of van Ruitenbeek et al. (2014) TRDR data are used and processed using a photometric and atmospheric correction and bad band removal. This is similar to this study, where MTRDR data are used that are already corrected for photometric and atmospheric influences and a bad band removal has been applied (Murchie et al., 2007). To judge the similarity in outcome the classification of CRISM image frt0000d6d6 using decision trees is compared to the result in van Ruitenbeek et al. (2014). In van Ruitenbeek et al. (2014) the wavelength of the deepest absorption features in the range of 2100-2400 nm is visualized using different color hues and the depth of the absorption features using different color intensities (Fig. 4.2.C). Despite the differences in classification of the image, the structure of the signals should be similar for both studies, as the mineral classification is partly based on the wavelength position of the deepest absorption feature.

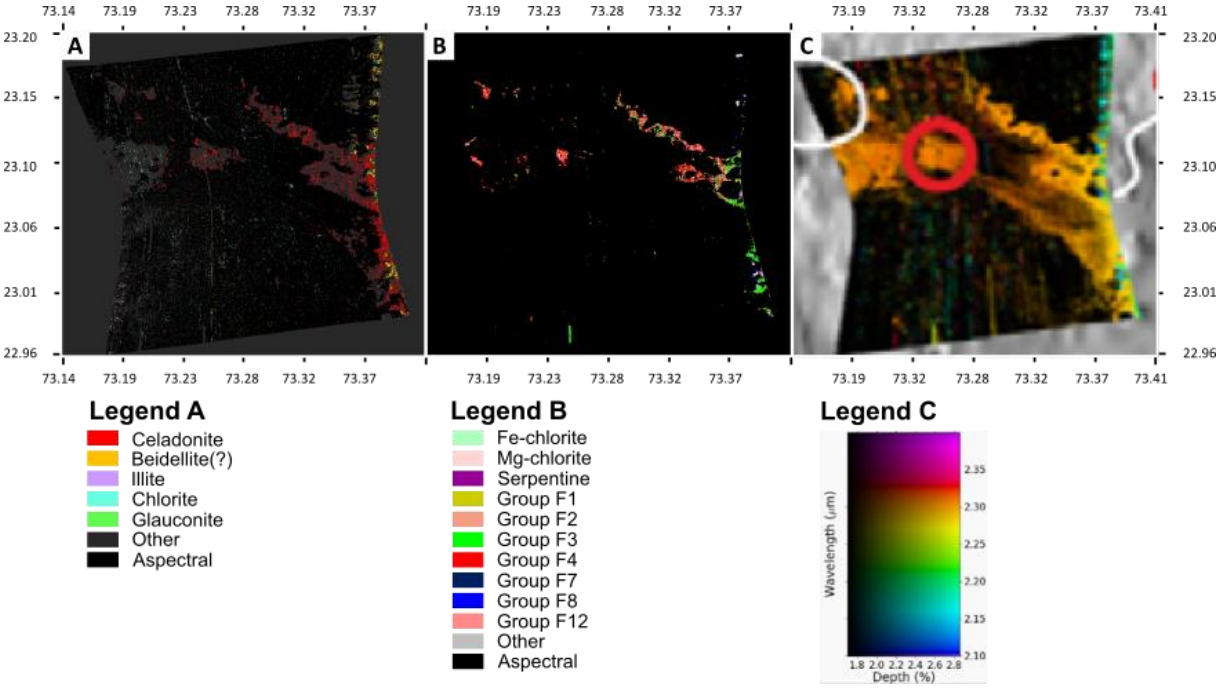

Fig. 4.3 CRISM image frt0000d6d6 in the Nili Fossae area.
A. Application of "Decision_tree_hydrothermal.tree", legend in Fig. A.1.3.I. B. Application of van Ruitenbeek (2021) decision tree for images with a wavelength range of 2100-2400 nm, legend in Fig. A.1.3.VI C. Visualization of the wavelength positions and depth of the deepest absorption feature (van Ruitenbeek et al., 2014). Legend A and B only include the minerals that are classified in these hyperspectral images. A complete legend and content of the groups is present in Fig. A.1.3 and table A.2.3. Legend C shows the color hue and intensity for different wavelength positions and depths (van Ruitenbeek et al., 2014).

The structure of the hydrous minerals classified by the developed decision tree is similar to the visualization of the deepest absorption features in van Ruitenbeek et al. (2014) (Fig. 4.3). Lower intensities and therefore absorption features with a smaller dip in reflectance in van Ruitenbeek (2021), are less well visualized in both classified images using decision trees (Fig. 4.3). In the classification after applying the developed decision tree different individual minerals are distinguished: celadonite, chlorite, glauconite, beidellite(?), and kaolinite. Furthermore, it gives a better overview of the present signals observed in van Ruitenbeek et al. (2014) compared to classification in mineral groups (Fig. 4.3). The presence of these individual minerals in Nili Fossae cannot be confirmed by comparison with (van Ruitenbeek et al., 2014), as no minerals are classified in this study. The classified individual minerals fit into the structure that is observed in the classification of van Ruitenbeek et al. (2014).

In future work, a combination of the developed decision tree and other decision trees can be applied to CRISM data to get an overview of the present hydrous minerals. However, more detailed comparisons with other studies are necessary to validate the classification of CRISM data in individual minerals.

4.4.4 Comparison with Brazilian analogues

In the Brazilian analogues the hydrothermal alteration is characterized by zeolites and quartz and minor presence of celadonite, beidellite(?), and calcite in white veins (sections 3.1, 3.2 and 3.4.1). Zeolites have not been distinguished in the classifications of the Martian impact structures using the developed and other decision trees (section 3.4.2). Furthermore, calcite is not specified in the classifications of Martian craters. The “Other” group included in the developed decision tree, in which all hydrous minerals with absorption features around 1400 nm and 1900 nm can be classified (Fig. A.1.1), could contain all the minerals observed in the white veins in the Brazilian impact structures. Illite and chlorite are distinguished by the developed decision tree in Toro and Auki crater, but not in the Brazilian craters (section 3.4). The absence of validation of classification of the Martian craters in individual minerals complicates comparison with the Brazilian analogues. The higher concentration of hydrous minerals around the center of Toro crater corresponds to the general distribution of hydrothermal alteration as described in Osinski et al. (2013) and the distribution observed in the Vargeão and Vista Alegre impact structures (Alsemgeest et al., 2021; Yokoyama et al., 2015). The minor amount of hydrous minerals in Auki (Fig. 3.7.B) and the lack of any clear hydrous signal in Canso and Laylá crater (Fig. A.1.4) is different from the observations of the Brazilian craters. Limitations of the developed decision tree (section 4.4) and implications on the comparability between Mars and Earth and the origin of the hydrothermal alteration (section 4.5) could explain these differences between hydrothermal alteration in Martian and Brazilian craters.

4.5 Limitations for application of the developed decision tree on Mars

The classifications of CRISM data after applying the developed decision tree and other decision trees (van Ruitenbeek, 2021) differs from classifications in other studies (section 4.4). The lack of hydrous minerals observed in the classifications of Canso and Laylá also differs from the observations of hydrothermal alteration in the Brazilian impact structures. Limitations of the decision tree and processing of CRISM data, and other influences, such as dust cover, could explain these differences. These limitations of the application of the decision trees on Mars are discussed below.

4.5.1 (Pre-)processing of CRISM data

Differences in processing steps and raw CRISM data could result into differences in mineral classification of CRISM images. The difference in classification of Auki crater between Carrozzo et al. (2017) and this study could be explained by the different method. Both studies use the CRISM image hrl000082e8, but the wavelength range and processing is different. In Carrozzo et al. (2017) the image

is used with a wavelength range of 400-4000 nm, while in this study images of 1000-2500 nm is used. A neutral component is subtracted in the spectra in Carrozzo et al. (2017) to remove systematic artifacts and to highlight spectral features, while this is not performed in this study. Using spectral ratios could reduce the influence of noise of the CRISM data to the classification. This different processing step could therefore explain the different classification between the two studies, as noise has a bigger influence on the images in this study. Striping and spectral smile in raw CRISM images could cause random scattering of hyperspectral signals in lines and on the edge of the image, which influences the classification (Naoto et al., 2010). Topographic, photometric, and atmospheric corrections are approximative and no thermal correction has been applied in this study (Seelos et al., 2011). This could cause systematic artifacts in the CRISM data and makes it difficult to apply decision trees, based on terrestrial samples, to the Martian data. So usage of spectral ratios, as seen in Carrozzo et al. (2017), is preferred when working with CRISM data, as these could eliminate some of systematic artifacts that are caused by approximative corrections during processing steps.

4.5.2 Topographical resolution

The size of Martian craters is in the order of 10^5 bigger than the Brazilian samples used to develop the decision tree (Fig. 3.6 and 3.7). This difference in topographical resolution of the classification images could cause differences in classified minerals. As one pixel in the CRISM data is 18 x 18 m or 32 x 32 m, while one pixel in the hyperspectral data from the Brazilian samples is 26 x 26 µm, chances on the presence of mixtures of different minerals per pixel from CRISM data are higher (sections 2.3.1 and 2.4). Therefore, the classifications of the Brazilian samples are more detailed and precise compared to the classifications of Martian craters. This can explain the higher amount of classified individual minerals in the Brazilian samples, as more pixels of the CRISM data could consist of a mixture of minerals and are therefore classified as “Other” by the developed decision tree or classified in a mineral group.

The lack of hydrous minerals in the classifications of Canso and Laylá crater can also be explained by this topographical resolution difference. As there is a higher amount of hydrothermal alteration necessary to classify a pixel as a hydrous mineral, most pixels of craters with a small amount of hydrothermal alteration will be classified as aspectral.

Auki crater is the only selected crater with a topographical resolution of 26 m/pixel instead of 18 m/pixel. A lower spatial resolution causes a strong decrease in detections of hydrous minerals (Carter et al., 2013). The smaller amount of hydrothermal alteration observed in the classification of Auki crater compared to Toro crater (section 4.4), which has a higher spatial resolution of 18 m/pixel, corresponds to this observation (Carter et al., 2013). However, the lack of signals in Canso and Laylá crater, which both have a higher spatial resolution of 18 m/pixel than Auki crater, does not correspond with the observations by Carter et al. (2013), because a higher amount of detections of hydrous minerals for Canso and Laylá crater compared to Auki crater would be expected.

4.5.3 Dust cover

The lack of clear signals of hydrous minerals in the Canso and Laylá crater can be caused by dust cover in the crater. A dust cover thicker than only a few tens to hundreds of micrometers can already mask any signal from the underlying bedrock (Carter et al., 2013). With the Dust Cover Index (DCI) measured by the Thermal Emission Spectrometer (TES), an estimate on the influence of dust on the hyperspectral signals can be made (Ruff & Christensen, 2002). Canso and Toro are located in areas with relatively low emissivity, which correlates to a relatively high dust cover thickness, while Auki and Laylá show medium emissivity, which correlates to a medium dust cover thickness (Ruff & Christensen, 2002). In contrast to expectations from the DCI of Toro, the classification of Toro crater shows most hydrous signals from the hyperspectral data (Fig. 4.1). As a result of the low resolution of the DCI map, the map could give wrong DCI estimates at the locations of the craters, but there could also be other causes for the lack of signal in the Laylà and Canso crater.

4.6 Implications for Mars

Other suggestions that could cause differences between the Martian and Brazilian mineral classifications and classifications from other studies, such as origin differences of hydrothermal alteration and possible errors in the selected analogous crater size, are discussed below.

4.6.1 Excavated and impact-generated hydrothermal alteration

Differences in origin of hydrothermal alteration could cause classification differences between Mars and Earth. It is suggested that the red veins in the Vargeão Dome and Vista Alegre impact structures have an impact-generated origin, while the white veins are formed pre-impact and brought to the surface as a result of excavation during impact (Alsemgeest et al., 2021; Yokoyama et al., 2015). Therefore, the origin of the white veins could not be related to the impact event.

Excavation of hydrous minerals is observed on Mars by the presence of hydrous minerals in the crater rim and ejecta blanket (Carter et al., 2011; Osinski et al., 2013). At more complex craters (partial) overprinting of the excavated altered materials can take place by impact-generated alteration (Osinski et al., 2013). Good estimates on impact ages and hydrothermal alteration ages are lacking and fail to exclude the origin of hydrothermal alteration. This makes it very difficult to distinguish excavated and impact-generated alteration. Therefore, the suggestions on the origin of observed hydrothermal alteration below are speculative.

The developed decision tree does not classify hydrous minerals in the red veins, but the other decision trees classify a higher concentration of illite and muscovite (section 4.3.2). This suggests that impact-generated hydrothermal alteration can include these phyllosilicates. Zeolite, celadonite, and beidellite(?), which are the main hydrous minerals present in the white veins (section 3.4.1), are likely excavated.

On Mars, no zeolite is classified using the developed decision tree (section 4.3.2), while the Brazilian samples contain a lot of zeolites (section 4.3.1), which suggests less excavation of hydrous minerals during impact in Martian craters, compared to the Brazilian analogues. A small amount of illite, chlorite, celadonite, and beidellite(?) is classified in Martian craters (section 3.4.2). The celadonite and beidellite(?) are likely excavated to the surface during impact, as these are also present in the white veins of the Brazilian impact craters. An impact-generated origin is suggested for illite, as this mineral is classified in the red veins of the Brazilian analogues, which are suggested to be impact-generated. Chlorite has not been observed in the Brazilian analogues and therefore the origin cannot be suggested.

This lack in knowledge of the origin of hydrothermal alteration makes comparison between Martian impact craters and the Brazilian analogues very difficult, as it is not clear whether the same generation of hydrothermal alteration is compared. The presence of illite and the lack of zeolites on Mars could suggest a dominant impact-generated origin of the observed hydrothermal alteration, while the origin of hydrothermal alteration in the Brazilian analogues is suggested to be mainly not related to the impact event.

4.6.2 Crater size

The selected analogous crater size range for Mars, 20-42 km in diameter (section 1.4.2), can be questioned, as only the largest selected craters Toro and Auki with a diameter of 42 and 38 km respectively, show signals of hydrous minerals (sections 4.4.1 and 4.4.2). A simulation of the post-impact hydrothermal system for a crater with a diameter of 45 km shows temperatures above 100 °C for more than 1000 years in the centermost 333 m and surface-exposed upper 200 m (Barnhart et al., 2010). Abramov and Kring (2005) show temperatures above 100 °C for more than 1000 years in a crater with a diameter of 30 km in the near surface up to 6 km from the crater center, which is not similar to the outcome of Barnhart et al. (2010). A temperature above 300 °C for more than 20,000 years is simulated for a crater with a diameter of 100 km in the near surface up to 15 km from the crater center (Abramov & Kring, 2005). After impact forming this big crater, temperatures can increase above 1000

°C and an impermeable melt sheet can originate in the center of the crater, which causes the hydrothermal system to be absent in the centermost ~10 km of the crater (Abramov & Kring, 2005).
Both simulations for the craters with a diameter of 30 and 45 km result in hydrothermal activity in the center (Abramov & Kring, 2005; Barnhart et al., 2010). Crater Toro matches with these simulations, as hydrous minerals are observed in the center of the crater (section 4.4.1). The difference between the post-impact temperature estimates of these studies are caused by the differences in model parameters, such as surface temperature and permeability. Rock permeability is an important factor for the amount of hydrothermal activity and can vary between different tholeiitic basalts (Abramov & Kring, 2005). Surface temperatures also vary over the Martian surface (Encrenaz et al., 1991).
All three simulations for crater diameters of 30, 45, and 100 km show suitable circumstances for a hydrothermal system to occur, when a water source is present (Kristmannsdottir, 1979). No information is found on the temperature and water fluxes for craters with a diameter smaller than 30 km. Bigger diameters of craters show larger hydrothermal systems with higher temperatures. However, surface temperature and mostly permeability have a big impact on the hydrothermal activity. More research is necessary into the influence of the crater size on the hydrothermal system and variation in surface temperature and permeability on Mars to indicate the minimum crater size, where hydrothermal alteration can form that can be observed using CRISM data.
The sample size of Martian craters in this study is small, which prevents from drawing firm conclusions. Therefore, more research into analogous crater sizes between Earth and Mars and Martian surface temperature and permeability is necessary. Within the limitations of this study, however, the minimum crater size is estimated to be around 30-40 km to observe hydrous minerals using CRISM data, as Laylá and Canso crater lack clear signals of hydrothermal alteration, while the larger Toro and Auki crater show signals of hydrothermal alteration (Fig. 3.7 and A.1.4).

5. Conclusion

To asses past presence of hydrothermal systems in Martian craters, a decision tree classifying individual minerals of hydrothermal alteration is developed. The developed decision tree is well applicable to terrestrial samples containing hydrothermal alteration. Especially zeolites and celadonite are well distinguishable in a classification using the developed decision tree. However, the developed decision tree fails to classify red veins and calcite. Therefore, it is recommended to apply a combination of decision trees, classifying both individual minerals and mineral groups, to the hyperspectral data of terrestrial samples to get a complete overview of the minerals and structures present.

Application of the developed decision tree on CRISM images can give an overview of hydrous minerals, mainly in common groups. However, these classifications lack details compared to other studies and for two of the four craters no signals of hydrothermal alteration are observed. More detailed comparison with other studies is necessary to validate the classification of CRISM data in individual minerals using the developed decision tree. The lack of signals for hydrothermal alteration and only a few classified individual minerals complicates the comparison with hydrothermal alteration in the Brazilian analogues. Zeolites and celadonite could be present in the common hydrous group that is observed in Toro crater, but can neither be confirmed or rejected. Craters Canso and Laylá lack signals of hydrothermal alteration and therefore do not compare to the Brazilian analogues.

There are at least four possible causes for the differences between the classifications of terrestrial samples and the Martian classifications, and between Martian classifications in this study and in other studies. Limitations of the (pre)processing of the CRISM data and of the decision tree could cause the lack of signals of hydrothermal alteration in Canso and Laylá crater. Furthermore, dust cover in Martian craters could explain a lack of signal in these craters. The higher topographical resolution of the Brazilian hyperspectral data compared to the CRISM data could explain differences between the hydrothermal alteration observed in the Brazilian and Martian classifications.
Illite, observed in Toro crater, is suggested to be impact-generated, as this mineral is also classified in the suggested impact-generated red veins of the Brazilian analogues. The lack of classified zeolites in Martian craters suggests that less excavation of hydrous minerals occurred during impacts in Martian craters, compared to the Brazilian analogues.
Finally, the lower amount of hydrothermal alteration in Martian craters compared to the Brazilian analogues could be explained by a possible incorrect selected size range for Martian craters to compare with terrestrial craters, when taking into account the gravity and surface pressure differences between Earth and Mars. This study could not detect hydrothermal alteration in Martian craters with a diameter <30 km. Therefore, it is suggested that the lower crater size limit for an impact-generated hydrothermal system to occur on Mars is around 30-40 km in diameter.

In conclusion, impact-generated hydrothermal systems most likely explain the occurrence of hydrous minerals in craters on Mars, as illite, which could be impact-generated, is observed in Toro crater, while zeolites, which are likely excavated, are not observed in selected Martian craters. However, an excavation origin for the classified Martian hydrous minerals cannot be excluded.

6. Recommendations

To improve the applicability of the decision tree on CRISM data it is recommended to use spectral ratios for elimination of systematic artefacts (section 4.5.1). The developed and other decision trees (van Ruitenbeek, 2021) can be combined in one complete decision tree to get classifications of a combination of individual minerals and mineral groups with a single analysis. The content of mineral groups can be adjusted based on the extent to which it is possible to distinguish between specific absorptions features in CRISM data, where signals can be affected by noise and mixed. Furthermore, it is useful to split the "Other" group of the developed decision tree in a hydrous and non-hydrous group to better distinguish these differences. It is useful to apply the developed decision tree on hyperspectral data collected by a rover on Mars to indicate the influence of difference in topographical resolution on the classification. More research into the influence of crater size, permeability, and surface temperature on hydrothermal systems for both Martian and terrestrial impact structures is necessary to better indicate comparable crater sizes. New research into age data of hydrothermal alteration and impact events could distinguish between an excavated or impact-generated origin. This is useful for the validation of simulations of hydrothermal systems and adds important information for comparison between Martian and terrestrial classifications of hydrothermal alteration. Further research into the clay content of the red veins in the Vista Alegre and Vargeão Dome impact structures is useful for comparison between Martian and Brazilian classifications.
Samples containing white and red veins, shatter cones, and impact breccias are collected from the Araguainha impact structure, in the Northeast of the Paraná basin, Brazil, during a fieldtrip in November 2022. This crater differs from the Vargeão Dome and Vista Alegre impact structures, as the crater has a higher diameter of ~40 km and an older age of 254.7 ± 2.5 Ma and is impacted into Paleozoic sedimentary rocks instead of basalts. Furthermore, the impact occurred during wet conditions, namely a shallow sea depositional environment (Engelhardt et al., 1992; Miyazaki et al., 2021; Tohver et al., 2012). After impact uplift of the complete stratigraphy occurred resulting in a bull's eye pattern around a granitic core, exposing the Furnas, Ponta Grossa, Aquidauana, and the Passa Dois Group (Miyazaki et al., 2021). The hydrothermal alteration observed in different exposed lithologies were collected. It is useful for the expansion and increase of applicability of the decision, to collect optical and scanning microscopy and hyperspectral data and add information of hydrothermal alteration in the sediments and granitic basement. Furthermore, cross-cutting relations between shatter cone structures and veins in samples where both features are present, could indicate an excavated or impact-generated origin of hydrothermal alteration. Finally, studying these samples could add to simulations of hydrothermal systems with different crater sizes and amount of water present, and indicate the influence of weathering and erosion on hydrothermal alteration.

7. Acknowledgements

First of all, I would like to thank my daily supervisor Jitse Alsemgeest for all the feedback, guidance throughout this project and making me familiar with useful programs. I have learned so many new things during this project and admire all your hard work. Special thanks to Frank Ruitenbeek for explaining the features in the Hyppy 3 Python extension and helping with collecting the hyperspectral data of the Brazilian samples. Furthermore, I would like to thank Jitse Alsemgeest and Juliette Faucher for being great company during our fieldtrip in Brazil. It was an amazing adventure and I am glad that I got to experience this with you. Also thanks to Alvaro Crósta, Natalia Hauser, and Uwe Reimold for the guidance during the fieldwork and helping communicate with the locals. I would like to express my gratitude to Fraukje Brouwer and Monica Sanchez Roman for being my first supervisor and second assessor and evaluate my research project. Lastly, I would like to thank Camiel, my parents, Mees, Loes, and Eva for enduring me when Hyppy did not run on my laptop, documents were not well saved and for searching articles when the VU had no access.

References

Abderrazak, B., Shahid, S., Alshankiti, A., El Battay, A., & Mohamed, N. (2018). *Hyperspectral signatures properties of a newly discovered anhydrite soil in united Arab Emirates and accepted by USDA soil taxonomy* IEEE-IGARSS-2018, Valencia, Spain.

Abramov, O., & Kring, D. A. (2005). Impact-induced hydrothermal activity on early Mars. *Journal of Geophysical Research: Planets*, *110*(E12). https://doi.org/https://doi.org/10.1029/2005JE002453

Alsemgeest, J., Brouwer, F. M., Auqué, L. F., Hauser, N., & Reimold, W. U. (2021). Hydrothermal alteration at the basalt-hosted Vista Alegre impact structure, Brazil. *Meteoritics & Planetary Science*, *56*(12), 2155-2174. https://doi.org/https://doi.org/10.1111/maps.13763

Alvares, C. A., Stape, J. L., Sentelhas, P. C., Gonçalves, J. d. M., & Sparovek, G. (2013). Köppen's climate classification map for Brazil. *Meteorologische zeitschrift*, *22*(6), 711-728. https://doi.org/10.1127/0941-2948/2013/0507

Anoop, A., Prasad, S., Plessen, B., Basavaiah, N., Gaye, B., Naumann, R., Menzel, P., Weise, S., & Brauer, A. (2013). Palaeoenvironmental implications of evaporative gaylussite crystals from Lonar Lake, central India. *Journal of Quaternary Science*, *28*(4), 349-359. https://doi.org/10.1002/jqs.2625

Arújo, L. M., França, A. B., & Potter, P. E. (1999). Hydrogeology of the Mercosul aquifer system in the Paraná and Chaco-Paraná Basins, South America, and comparison with the Navajo-Nugget aquifer system, USA. *Hydrogeology Journal*, *7*(3), 317-336. https://doi.org/10.1007/s100400050205

Bakker, W. H. (2018). HypPy User Manual.

Barnhart, C. J., Nimmo, F., & Travis, B. J. (2010). Martian post-impact hydrothermal systems incorporating freezing. *Icarus*, *208*(1), 101-117. https://doi.org/10.1016/j.icarus.2010.01.013

Baross, J. A., & Deming, J. W. (1983). Growth of 'black smoker' bacteria at temperatures of at least 250 °C. *Nature*, *303*(5916), 423-426. https://doi.org/10.1038/303423a0

Bishop, J. L., Lane, M. D., Dyar, M. D., & Brown, A. J. (2008). Reflectance and emission spectroscopy study of four groups of phyllosilicates: smectites, kaolinite-serpentines, chlorites and micas. *Clay Minerals*, *43*(1), 35-54. https://doi.org/10.1180/claymin.2008.043.1.03

Bowitz, J. r., & Ehling, A. (2008). Non-destructive infrared analyses: A method for provenance analyses of sandstones. *Environmental Geology*, *56*, 623-630. https://doi.org/10.1007/s00254-008-1361-6

Buller, D. (2023). *envi: Environmental Interpolation using Spatial Kernel*. In The Comprehensive R Archive Network. https://cran.r-project.org/package=envi

Carrozzo, F. G., Di Achille, G., Salese, F., Altieri, F., & Bellucci, G. (2017). Geology and mineralogy of the Auki Crater, Tyrrhena Terra, Mars: A possible post impact-induced hydrothermal system. *Icarus*, *281*, 228-239. https://doi.org/10.1016/j.icarus.2016.09.001

Carter, J., Poulet, F., Bibring, J. P., Mangold, N., & Murchie, S. (2013). Hydrous minerals on Mars as seen by the CRISM and OMEGA imaging spectrometers: Updated global view. *Journal of Geophysical Research: Planets*, *118*(4), 831-858. https://doi.org/10.1029/2012JE004145

Carter, J. A., Poulet, F., Loizeau, D., Bibring, J.-P., & Murchie, S. (2011, March 01, 2011). *Impact Craters as Probes to Investigate the Upper Crustal Hydrous Mineralogy on Mars* 42nd Lunar and Planetary Science Conference, The Woodlands, Texas. https://ui.adsabs.harvard.edu/abs/2011LPI....42.2619C

Chatterjee, S. (2016). A symbiotic view of the origin of life at hydrothermal impact crater-lakes. *Physical Chemistry Chemical Physics*, *18*(30), 20033-20046. https://doi.org/10.1039/C6CP00550K

Cloutis, E. A., Asher, P. M., & Mertzman, S. A. (2002). Spectral reflectance properties of zeolites and remote sensing implications. *Journal of Geophysical Research: Planets*, *107*(E9), 5-1-5-19. https://doi.org/10.1029/2000JE001467

Cockell, C. S. (2006). The origin and emergence of life under impact bombardment. *Philosophical Transactions of the Royal Society B: Biological Sciences*, *361*(1474), 1845-1856. https://doi.org/10.1098/rstb.2006.1908

Cockell, C. S., Osinski, G. R., & Lee, P. (2003). The impact crater as a habitat: effects of impact processing of target materials. *Astrobiology*, *3*(1), 181-191. https://doi.org/10.1089/153110703321632507

Crósta, A. P., Kazzuo-Vieira, C., Pitarello, L., Koeberl, C., & Kenkmann, T. (2011). Geology and impact features of Vargeão Dome, southern Brazil. *Meteoritics & Planetary Science*, *47*(1), 51-71. https://doi.org/10.1111/j.1945-5100.2011.01312.x

Crósta, A. P., Koeberl, C., Furuie, R. A., & Kazzuo-Vieira, C. (2010). The first description and confirmation of the Vista Alegre impact structure in the Paraná flood basalts of southern Brazil. *Meteoritics & Planetary Science*, *45*(2), 181-194. https://doi.org/10.1111/j.1945-5100.2010.01015.x

Dypvik, H., Hellevang, H., Krzesínska, A., Sætre, C., Viennet, J.-C., Bultel, B., Ray, D., Poulet, F., Loizeau, D., Veneranda, M., Rull, F., Cousin, A., & Werner, S. C. (2021). The Planetary Terrestrial Analogues Library (PTAL) – An exclusive lithological selection of possible martian earth analogues. *Planetary and Space Science*, *208*, 105339. https://doi.org/10.1016/j.pss.2021.105339

Ehlmann, B. L., Mustard, J. F., Swayze, G. A., Clark, R. N., Bishop, J. L., Poulet, F., Des Marais, D. J., Roach, L. H., Milliken, R. E., Wray, J. J., Barnouin-Jha, O., & Murchie, S. L. (2009). Identification of hydrated silicate minerals on Mars using MRO-CRISM: Geologic context near Nili Fossae and implications for aqueous alteration. *Journal of Geophysical Research: Planets*, *114*(E2). https://doi.org/10.1029/2009JE003339

Encrenaz, T., Lellouch, E., Rosenqvist, J., & Bouchet, P. (1991). A determination of albedos and surface temperatures on Mars from ground-based infrared spectroscopy. *Planetary and Space Science*, *39*(1), 267-272. https://doi.org/10.1016/0032-0633(91)90148-4

Engelhardt, W. V., Matthäi, S. K., & Walzebuck, J. (1992). Araguainha impact crater, Brazil. I. The interior part of the uplift. *Meteoritics*, *27*(4), 442-457. https://doi.org/10.1111/j.1945-5100.1992.tb00226.x

Fairén, A. G., Marzo, G. A., Chevrier, V., Gavin, P., Davila, A. F., Gross, C., Kneissl, T., Roush, T. L., Bishop, J. L., Dohm, J. M., Tornabene, L. L., & McKay, C. P. (2010, 2010/04/1). *Toro Crater: The Case for Hesperian Phyllosilicates on Mars* Astrobiology Science Conference 2010, Houston, Texas. https://ui.adsabs.harvard.edu/abs/2010LPICo1538.5588F

Feldman, V., Sazonova, L., Mironov, Y. V., Kapustkina, I., & Ivanov, B. (1983). *Circular structure Logancha as possible meteorite crater in basalts of the Tunguska syneclise* Lunar and Planetary Science Conference, https://adsabs.harvard.edu/full/1983LPI....14..191F

Fredriksson, K., Dube, A., Milton, D., & Balasundaram, M. (1973). Lonar Lake, India: An impact crater in basalt. *Science*, *180*(4088), 862-864. https://doi.org/10.1126/science.180.4088.862

Gonçalves, R. D., Teramoto, E. H., & Chang, H. K. (2020). Regional Groundwater Modeling of the Guarani Aquifer System. *Water*, *12*(9). https://doi.org/10.3390/w12092323

Grizonnet, M., Michel, J., Poughon, V., Inglada, J., Savinaud, M., & Cresson, R. (2017). Orfeo ToolBox: open source processing of remote sensing images. *Open Geospatial Data, Software and Standards*, *2*(1), 15. https://doi.org/10.1186/s40965-017-0031-6

Guinness, E. A., Arvidson, R. E., Jolliff, B. L., Seelos, K. D., Seelos, F. P., Ming, D. W., Morris, R. V., & Graff, T. G. (2007). Hyperspectral reflectance mapping of cinder cones at the summit of Mauna Kea and implications for equivalent observations on Mars. *Journal of Geophysical Research: Planets*, *112*(E8). https://doi.org/10.1029/2006JE002822

Henley, R. W., & Ellis, A. J. (1983). Geothermal systems ancient and modern: a geochemical review. *Earth-Science Reviews*, *19*(1), 1-50. https://doi.org/10.1016/0012-8252(83)90075-2

Kieffer, H. H., Jakosky, B. M., & Snyder, C. W. M., Mildred Shapley (1992). *Mars: Maps* (Vol. 1). University of Arizona Press. https://uapress.arizona.edu/book/mars-2

Kokaly, R. F., Clark, R. N., Swayze, G. A., Livo, K. E., Hoefen, T. M., Pearson, N. C., Wise, R. A., Benzel, W. M., Lowers, H. A., Driscoll, R. L., & Klein, A. J. (2017). *USGS Spectral Library Version 7*. https://doi.org/10.3133/ds1035

Komor, S. C., Valley, J. W., & Brown, P. E. (1988). Fluid-inclusion evidence for impact heating at the Siljan Ring, Sweden. *Geology*, *16*(8), 711-715. https://doi.org/10.1130/0091-7613(1988)016%3C0711:FIEFIH%3E2.3.CO;2

Kristmannsdottir, H. (1979). Alteration of Basaltic Rocks by Hydrothermal-Activity at 100-300°C. In M. M. Mortland & V. C. Farmer (Eds.), *Developments in Sedimentology* (Vol. 27, pp. 359-367). Elsevier. https://doi.org/10.1016/S0070-4571(08)70732-5

Larsen, S. E., Jørgensen, H. E., Landberg, L., & Tillman, J. E. (2002). Aspects Of The Atmospheric Surface Layers On Mars And Earth. *Boundary-Layer Meteorology*, *105*(3), 451-470. https://doi.org/10.1023/A:1020338016753

Leovy, C. (2001). Weather and climate on Mars. *Nature*, *412*(6843), 245-249. https://doi.org/10.1038/35084192

Malin, M. C., Bell III, J. F., Cantor, B. A., Caplinger, M. A., Calvin, W. M., Clancy, R. T., Edgett, K. S., Edwards, L., Haberle, R. M., & James, P. B. (2007). Context camera investigation on board the Mars Reconnaissance Orbiter. *Journal of Geophysical Research: Planets*, *112*(E5). https://doi.org/10.1029/2006JE002808

Martin, W., Baross, J., Kelley, D., & Russell, M. J. (2008). Hydrothermal vents and the origin of life. *Nature Reviews Microbiology*, *6*(11), 805-814. https://doi.org/10.1038/nrmicro1991

Marzo, G. A., Davila, A. F., Tornabene, L. L., Dohm, J. M., Fairén, A. G., Gross, C., Kneissl, T., Bishop, J. L., Roush, T. L., & McKay, C. P. (2010). Evidence for Hesperian impact-induced hydrothermalism on Mars. *Icarus*, *208*(2), 667-683. https://doi.org/10.1016/j.icarus.2010.03.013

Masaitis, V. (2010). Impact structures of northeastern Eurasia: The territories of Russia and adjacent countries. *Meteoritics & Planetary Science*, *34*(5), 691-711. https://doi.org/10.1111/j.1945-5100.1999.tb01381.x

McSween, H. Y., Taylor, G. J., & Wyatt Michael, B. (2009). Elemental Composition of the Martian Crust. *Science*, *324*(5928), 736-739. https://doi.org/10.1126/science.1165871

Miyazaki, M. R., Leite, E. P., Vasconcelos, M. A. R., Wünnemann, K. A. I., & Crósta, A. P. (2021). Bouguer anomaly inversion and hydrocode modeling of the central uplift of the Araguainha impact structure. *Anais da Academia Brasileira de Ciências*, *93*(suppl 4). https://doi.org/10.1590/0001-3765202120210081

Murchie, S., Arvidson, R., Bedini, P., Beisser, K., Bibring, J. P., Bishop, J., Boldt, J., Cavender, P., Choo, T., Clancy, R. T., Darlington, E. H., Des Marais, D., Espiritu, R., Fort, D., Green, R., Guinness, E., Hayes, J., Hash, C., Heffernan, K., & Wolff, M. (2007). Compact Reconnaissance Imaging Spectrometer for Mars (CRISM) on Mars Reconnaissance Orbiter (MRO). *Journal of Geophysical Research*, *112*(E5). https://doi.org/10.1029/2006JE002682

Naoto, Y., Norihide, M., & Akira, I. (2010). *Preprocessing of hyperspectral imagery with consideration of smile and keystone properties* Proc.SPIE, https://doi.org/10.1117/12.870437

Nazari-Sharabian, M., Aghababaei, M., Karakouzian, M., & Karami, M. (2020). Water on Mars–A literature review. *Galaxies*, *8*(2), 40. https://doi.org/10.3390/galaxies8020040

Osinski, G. R., Tornabene, L. L., Banerjee, N. R., Cockell, C. S., Flemming, R., Izawa, M. R. M., McCutcheon, J., Parnell, J., Preston, L. J., Pickersgill, A. E., Pontefract, A., Sapers, H. M., & Southam, G. (2013). Impact-generated hydrothermal systems on Earth and Mars. *Icarus*, *224*(2), 347-363. https://doi.org/10.1016/j.icarus.2012.08.030

Pike, R. J. (1980). *Control of crater morphology by gravity and target type-Mars, Earth, Moon* Lunar and Planetary Science Conference, Houston. https://adsabs.harvard.edu/full/1980LPSC...11.2159P

Pillay, R., Picollo, M., Hardeberg, J. Y., & George, S. (2020). Evaluation of the Data Quality from a Round-Robin Test of Hyperspectral Imaging Systems. *Sensors*, *20*(14). https://doi.org/10.3390/s20143812

Pirajno, F. (1992). Fossil and Active Geothermal Systems — Epithermal Base and Precious Metal Mineralisation (Including Kuroko-Type Deposits). In *Hydrothermal Mineral Deposits.* Springer, Berlin. https://doi.org/10.1007/978-3-642-75671-9_12

Pirajno, F. (2009). *Hydrothermal processes and mineral systems*. Springer/Geological Survey of Western Australia. https://doi.org/10.2113/gsecongeo.104.4.597

QGIS_Development_Team. (2023). *QGIS Geographic Information System*. In QGIS Association. https://www.qgis.org

Rathbun, J. A., & Squyres, S. W. (2002). Hydrothermal Systems Associated with Martian Impact Craters. *Icarus*, *157*(2), 362-372. https://doi.org/10.1006/icar.2002.6838

Ruff, S. W., & Christensen, P. R. (2002). Bright and dark regions on Mars: Particle size and mineralogical characteristics based on Thermal Emission Spectrometer data. *Journal of Geophysical Research: Planets*, *107*(E12), 2-1-2-22. https://doi.org/10.1029/2001JE001580

Sagan, C. (1994). The Search for Extraterrestrial Life. *Scientific American*, *271*(4), 92-99. http://www.jstor.org/stable/24942874

Schwenzer, S. P., Abramov, O., Allen, C. C., Bridges, J. C., Clifford, S. M., Filiberto, J., Kring, D. A., Lasue, J., McGovern, P. J., Newsom, H. E., Treiman, A. H., Vaniman, D. T., Wiens, R. C., & Wittmann, A. (2012). Gale Crater: Formation and post-impact hydrous environments. *Planetary and Space Science*, *70*(1), 84-95. https://doi.org/10.1016/j.pss.2012.05.014

Seelos, F. P., Murchie, S. L., Humm, D. C., Barnouin, O. S., Morgan, F., Taylor, H. W., Hash, C., & Team, C. (2011, March 01, 2011). *CRISM Data Processing and Analysis Products Update — Calibration, Correction, and Visualization* 42nd Lunar and Planetary Science Conference, The Woodlands. https://ui.adsabs.harvard.edu/abs/2011LPI....42.1438S

Stewart, S., O'Keefe, J., & Ahrens, T. (2001). *The relationship between rampart crater morphologies and the amount of subsurface ice* Lunar and Planetary Science Conference, Houston. https://www.researchgate.net/publication/252283494_The_Relationship_Between_Rampart_Crater_Morphologies_and_the_Amount_of_Subsurface_Ice

Taylor, G. J., Martel, L. M. V., Karunatillake, S., Gasnault, O., & Boynton, W. V. (2010). Mapping Mars geochemically. *Geology*, *38*(2), 183-186. https://doi.org/10.1130/G30470.1

Tohver, E., Lana, C., Cawood, P. A., Fletcher, I. R., Jourdan, F., Sherlock, S., Rasmussen, B., Trindade, R. I. F., Yokoyama, E., Souza Filho, C. R., & Marangoni, Y. (2012). Geochronological constraints on the age of a Permo-Triassic impact event: U-Pb and $^{40}Ar/^{39}Ar$ results for the 40 km Araguainha structure of central Brazil. *Geochimica et Cosmochimica Acta*, *86*, 214-227. https://doi.org/10.1016/j.gca.2012.03.005

van Ruitenbeek, F. J. A. (2021). *Hyperspectral classification using wavelength mapping and decision trees: Frank's Tutorials*. https://youtu.be/NXItJJ8jfm0

van Ruitenbeek, F. J. A., Bakker, W. H., van der Werff, H. M. A., Zegers, T. E., Oosthoek, J. H. P., Omer, Z. A., Marsh, S. H., & van der Meer, F. D. (2014). Mapping the wavelength position of deepest absorption features to explore mineral diversity in hyperspectral images. *Planetary and Space Science*, *101*, 108-117. https://doi.org/10.1016/j.pss.2014.06.009

Vasconcelos, M. A. R., Rocha, F. F., Crósta, A. P., Wünnemann, K., Güldemeister, N., Leite, E. P., Ferreira, J. C., & Reimold, W. U. (2019). Insights about the formation of a complex impact structure formed in basalt from numerical modeling: The Vista Alegre structure, southern Brazil. *Meteoritics & Planetary Science*, *54*(10), 2373-2383. https://doi.org/10.1111/maps.13298

Wray, J. J., Murchie, S. L., Squyres, S. W., Seelos, F. P., & Tornabene, L. L. (2009). Diverse aqueous environments on ancient Mars revealed in the southern highlands. *Geology*, *37*(11), 1043-1046. https://doi.org/10.1130/G30331A.1

Yokoyama, E., Nédélec, A., Baratoux, D., Trindade, R. I. F., Fabre, S., & Berger, G. (2015). Hydrothermal alteration in basalts from Vargeão impact structure, south Brazil, and

implications for recognition of impact-induced hydrothermalism on Mars. *Icarus*, *252*, 347-365. https://doi.org/10.1016/j.icarus.2015.02.001

Zhou, K.-F., & Wang, S.-S. (2017). Spectral properties of weathered and fresh rock surfaces in the Xiemisitai metallogenic belt, NW Xinjiang, China. *Open Geosciences*, *9*, 27. https://doi.org/10.1515/geo-2017-0027

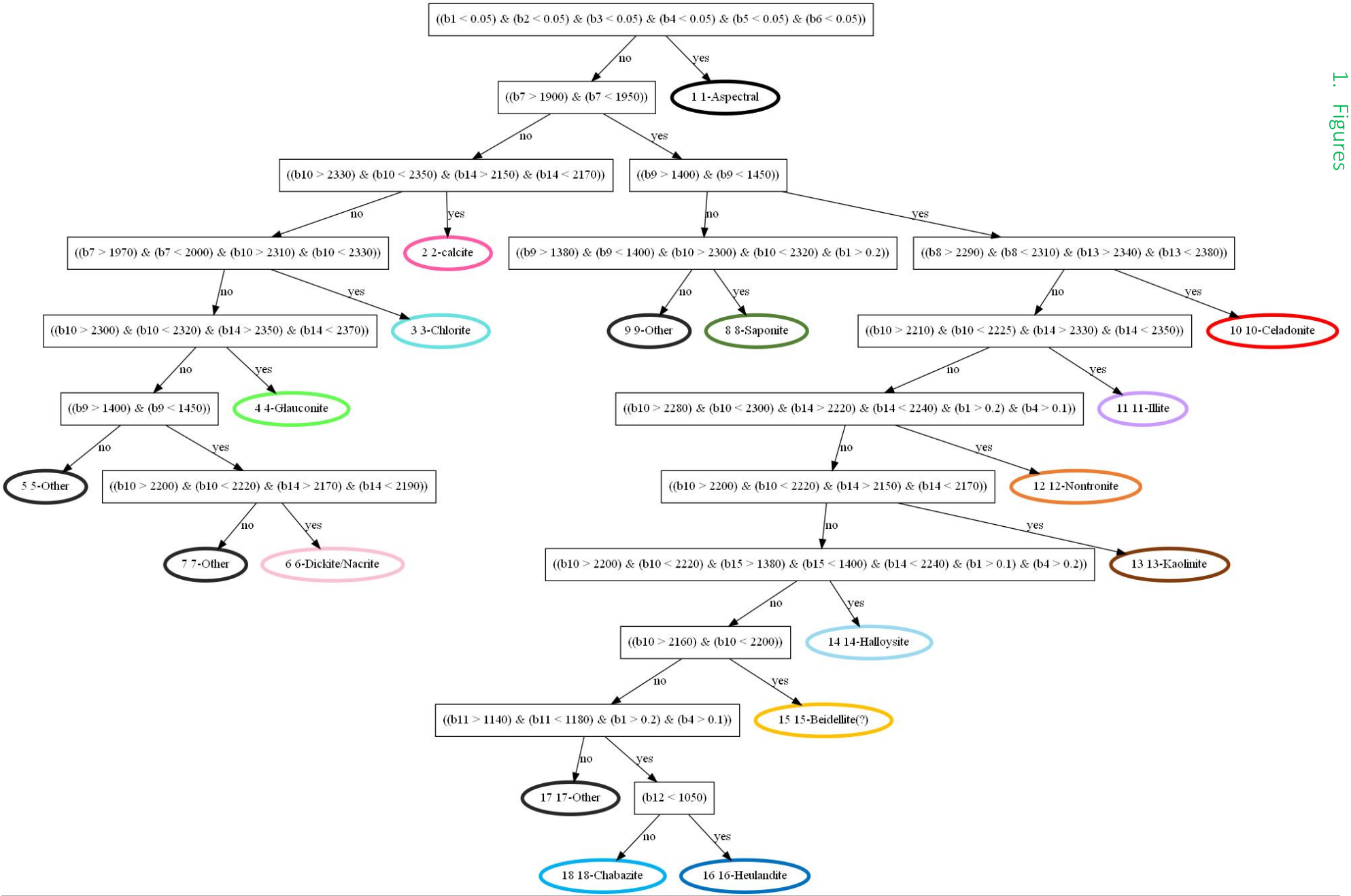

Fig. A.1.1 Dotplot of the designed decision tree to indicate hydrothermal alteration based on absorption features of the USGS spectral library. b1-b15 are defined in table A.2.1.

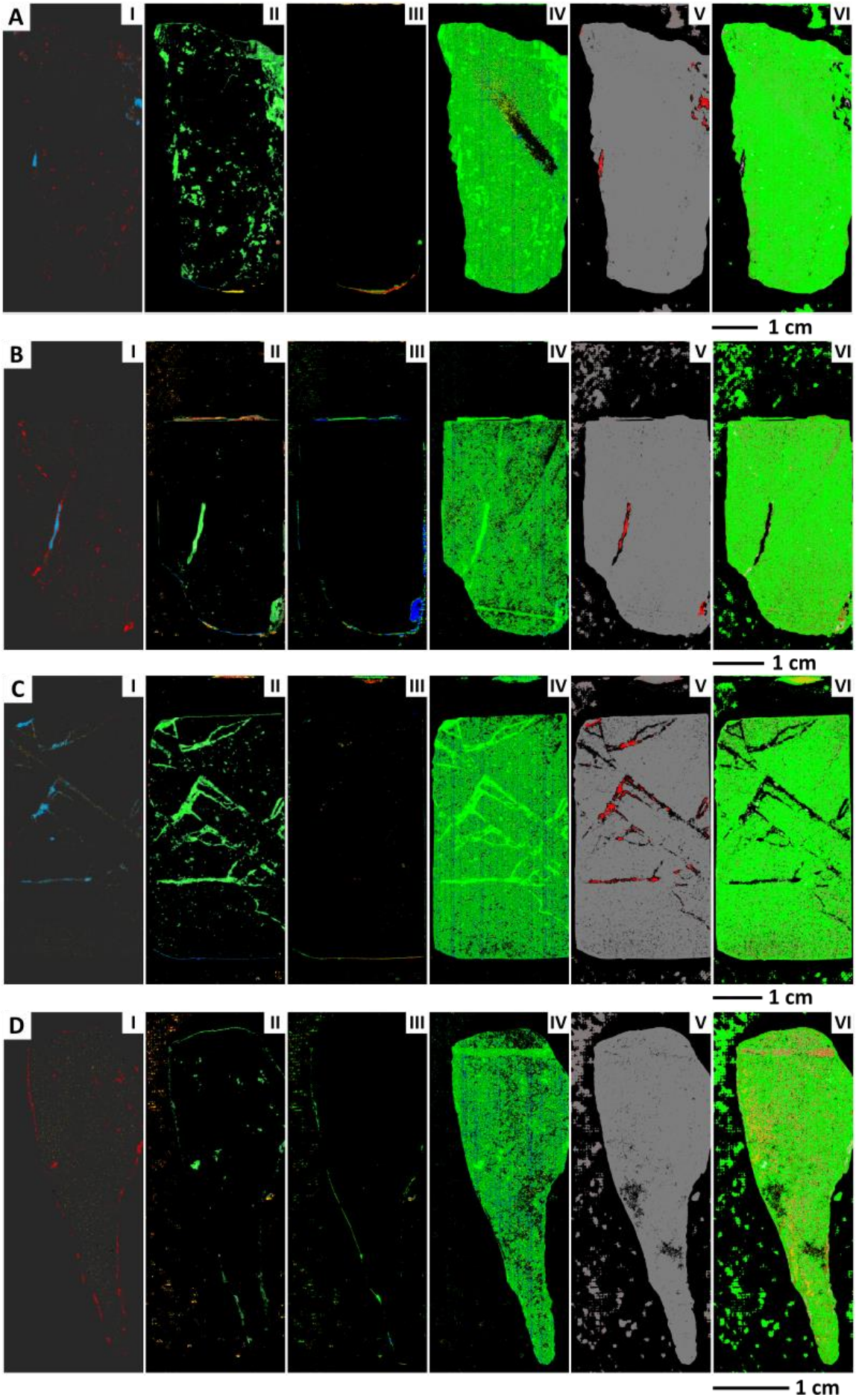
A
I
II
III
IV
V
VI
1 cm
B
I
II
III
IV
V
VI
1 cm
C
I
II
III
IV
V
VI
1 cm
D
I
II
III
IV
V
VI
1 cm

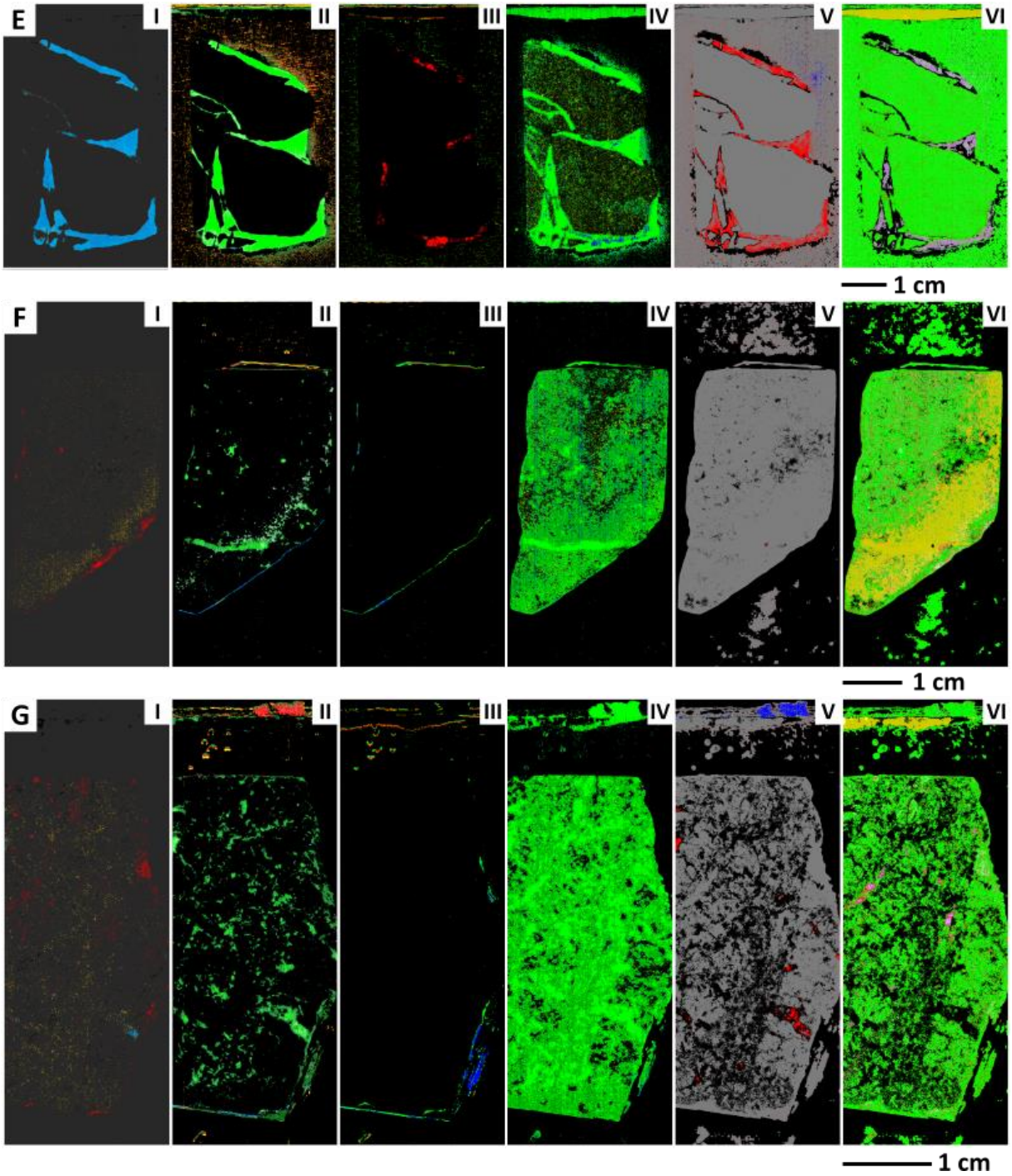

Fig. A.1.2 A. Mineral classification of sample VG1A. B. Mineral classification of sample VG2. C. Mineral classification of sample VG12. D. Mineral classification of sample VG20. E. Mineral classification of sample VG25. F. Mineral classification of sample VG28B. G. Mineral classification of sample VA92. I. Application of "Decision_tree_hydrothermal.txt" II. Application of van Ruitenbeek (2021) decision tree for images with a wavelength range of 1300-1600 µm III. of 1650-1850 µm. IV. of 1850-2100 µm. V. of 2000-2500 µm. VI. of 2100-2400 µm (van Ruitenbeek, 2021).

Fig. A.1.3 Complete legend with the mineral classes and groups for I. Application of "Decision_tree_hydrothermal.tree" II. Application of van Ruitenbeek (2021) decision tree for images with a wavelength range of 1300-1600 µm III. of 1650-1850 µm. IV. of 1850-2100 µm. V. of 2000-2500 µm. VI. of 2100-2400 µm. (van Ruitenbeek, 2021). An overview of the minerals in different groups is present in table A.2.3.

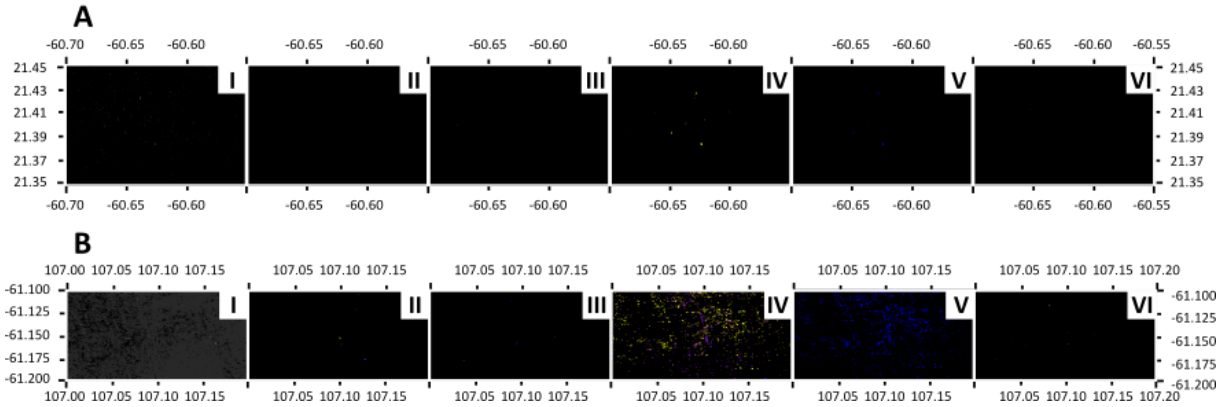

Fig. A.1.4 A. Mineral classification of Canso crater. B. Mineral classification of Laylá crater. I. Application of "Decision_tree_hydrothermal.txt" II. Application of van Ruitenbeek (2021) decision tree for images with a wavelength range of 1300-1600 µm III. of 1650-1850 µm. IV. of 1850-2100 µm. V. of 2000-2500 µm. VI. of 2100-2400 µm. (van Ruitenbeek, 2021). The legend is fig. A.1.3.

2. Tables

Table A.2.1 Definitions of b1-b15 in Fig. A.1.1 that refer to depths or wavelength positions of absorption features in different wavelength maps

b1	Depth of deepest absorption feature in the wavelength map with a range of 1850-2100 nm
b2	Depth of deepest absorption feature in the wavelength map with a range of 2000-2500 nm
b3	Depth of deepest absorption feature in the wavelength map with a range of 2100-2400 nm
b4	Depth of deepest absorption feature in the wavelength map with a range of 1300-1600 nm
b5	Depth of deepest absorption feature in the wavelength map with a range of 1650-1850 nm
b6	Depth of deepest absorption feature in the wavelength map with a range of 1000-1500 nm
b7	Wavelength position of deepest absorption feature in the wavelength map with a range of 1850-2100 nm
b8	Wavelength position of deepest absorption feature in the wavelength map with a range of 2000-2500 nm
b9	Wavelength position of deepest absorption feature in the wavelength map with a range of 1300-1600 nm
b10	Wavelength position of deepest absorption feature in the wavelength map with a range of 2100-2400 nm
b11	Wavelength position of deepest absorption feature in the wavelength map with a range of 1000-1500 nm
b12	Wavelength position of 3rd deepest absorption feature in the wavelength map with a range of 1000-1500 nm
b13	Wavelength position of 2nd deepest absorption feature in the wavelength map with a range of 2000-2500 nm
b14	Wavelength position of 2nd deepest absorption feature in the wavelength map with a range of 2100-2400 nm
b15	Wavelength position of 2nd deepest absorption feature in the wavelength map with a range of 1850-2100 nm

Table A.2.2 Overview of minerals present in white and red veins per selected sample based on optical and scanning electron microscopy data.

Sample	Minerals in veins
1A	Red vein: oxides, chabazite, plagioclase, pyroxene
2	Red vein: oxides, quartz, chabazite, plagioclase, pyroxene
	White vein: chabazite, quartz, clays
8	White vein: chabazite, clays
12	White vein: chabazite, clays
18	White vein: chabazite, quartz
20	Red vein: oxides, quartz, chabazite, plagioclase, pyroxene
25	White vein: chabazite, quartz
28B	White vein: chabazite, quartz
92	White vein: chabazite, quartz, calcite

Table A.2.3 Overview of mineral presence and possible hydrothermal alteration per sample (van Ruitenbeek et al., 2014).

Group B1	Halloysite; kaolinite; dickite
Group B2	Alunite; montmorillonite; analcime; zeolites
Group B3	Opal; chalcedony; goethite (?); gypsum; topaz; hydrogrossular; cordierite; tourmaline; glaucophane; muscovite; illite; microcline; olivine
Group B4	Siderite; sillimanite; olivine; amphibole; brucite; talc; pyrophyllite; vermiculite; phlogopite; serpentine; saponite
Group B5	Gibbsite; jarosite; prehnite; acmite
Group B6	Epidote; azurite
Group C1	Monazite; azurite; gypsum
Group C2	Alunite; hyperstene; analcime
Group C3	Epidote; beryll; natrolite; kaolinite
Group D1	Opal; goethite; dolomite (?) jarosite; alunite; vesuvianite; halloysite; kaolinite; chlorite; muscovite; illite; chrysotile; analcime; nepheline; zeolites
Group D2	Serpentine; glauconite; chlorite; hyperstene; epidote; jarosite
Group D3	Talc; illite; montmorillonite; beryll; cordierite
Group D4	Calcite; azurite; malachite; rodochrosite; chlorite
Group E1	Absorption feature located > 2400 nm
Group E2	Absorption feature located in between 2100 and 2400 nm
Group E3	Absorption feature located < 2100 nm
Group F1	Opal; chalcedony; goethite(?); gypsum; vesuvianite; tourmaline; cordierite; halloysite; montmorillonite
Group F2	Muscovite; illite
Group F3	Nontronite; chlorite; zoisite; malachite; azurite; gibbsite; jarosite
Group F4	Dolomite; brucite; pyroxene; glauconite; antigorite; Fe-Mg-smectite
Group F5	Calcite; spessartime; grossular; amphibole; vermiculite; phlogopite
Group F6	Calcite; rodochrosite; strotionite; Fe-chlorite; riebeckite
Group F7	Topaz; beryl; zunyite
Group F8	Alunite; dickite
Group F9	Sillimanite; paragonite; muscovite; natrolite; microcline; albite
Group F10	Muscovite; illite
Group F11	Opal; chalcedony; goethite (?); gypchlorsum; vesuvianite; tourmaline; cordierite; halloysite; montmorillonite
Group F12	Amphibole; talc
Group F13	Epidote; chlorite

Table A.2.4 Overview of mineral presence and possible hydrothermal alteration of the complete sample set based on optical and scanning electron microscopy data.

Sample	Minerals	Hydrothermal alteration
1A.2	Plagioclase, pyroxene, oxides	Red veins
1A.4	Plagioclase, pyroxene, quartz, clay, oxides	Quartz vein
1B	Plagioclase, pyroxene, kalifeldspar, oxides, chabazite, clay	Chabazite/clay veins, red vein
2	Plagioclase, pyroxene, oxides, quartz, clay	Quartz/clay veins, red vein
4B	Quartz	
6	Plagioclase, pyroxene, quartz, oxides	Quartz vein
8	Plagioclase, pyroxene, quartz, ilmenite, calciumphosphate, chabazite, clay	Chabazite/clay veins
9	Plagioclase, pyroxene, quartz, kalifeldspar, ilmenite, clay	Quartz/clay veins
12	Plagioclase, pyroxene, quartz, kalifeldspar, ilmenite, calciumphosphate, chabazite, clay	Chabazite/clay veins, red vein
14	Plagioclase, pyroxene, oxides, chabazite, clay	Chabazite vein
18	Plagioclase, pyroxene, quartz, ilmenite, calciumphosphate, chabazite	Chabazite/quartz veins
20	Plagioclase, pyroxene, quartz, kalifeldspar, ilmenite	Red vein
24*	Plagioclase, pyroxene, quartz, oxides	(breccia)
25	Plagioclase, pyroxene, quartz, ilmenite, chabazite	Chabazite/quartz veins
25B*	Plagioclase, pyroxene, oxides	(breccia)
28A	Plagioclase, pyroxene, quartz, oxides	Quartz veins
28B	Plagioclase, pyroxene, oxides	Chabazite/quartz vein
33	Plagioclase, pyroxene, kalifeldspar, clay, ilmenite, calciumphosphate	
34	Plagioclase, pyroxene, kalifeldspar, ilmenite	
35*	Plagioclase, pyroxene, quartz, oxides	(breccia)
40	Plagioclase, pyroxene, quartz, oxides, chabazite, clay	Chabazite/quartz/clay veins
47A	Plagioclase, pyroxene, quartz, oxides, chabazite, clay	Chabazite/quartz/clay veins
48*	Plagioclase, pyroxene, quartz, kalifeldspar, ilmenite, calciumphosphate	(breccia)
51*	Pyroxene, kalifeldspar, quartz, oxides, clay	Quartz/clay veins
53.1	Plagioclase, pyroxene, oxides	
53.2	Quartz, calcite	Quartz/calcite vein
56	Plagioclase, pyroxene, oxides	Red veins
80A	Plagioclase, pyroxene, ironoxide, chabazite, calcite	Chabazite/calcite veins
92.1	Plagioclase, pyroxene, kalifeldspar, quartz, ironoxide, calciumphosphate, calcite	Calcite veins